Preprint typeset using LaTeX style emulateapj v. 11/12/01

AN EXPANDED *RXTE* SURVEY OF LONG-TERM X-RAY VARIABILITY IN SEYFERT 1 GALAXIES

A. Markowitz[1], R. Edelson[2]

[1] Laboratory for High-Energy Astophysics, NASA/Goddard Space Flight Center, Code 662, Greenbelt, MD 20771; agm@milkyway.gsfc.nasa.gov
[2] Dept. of Astronomy, Univ. of California, Los Angeles CA 90095-1562; rae@astro.ucla.edu

ABSTRACT

The first seven years of *RXTE* monitoring of Seyfert 1 active galactic nuclei have been systematically analyzed to yield five homogenous samples of 2–12 keV light curves, probing hard X-ray variability on successively longer durations from ∼1 day to ∼3.5 years. 2–10 keV variability on time scales of ∼1 day, as probed by *ASCA*, are included. All sources exhibit stronger X-ray variability towards longer time scales, with variability amplitudes saturating at the longest time scales, but the increase is greater for relatively higher luminosity sources. The well-documented anticorrelation between variability amplitude and luminosity is confirmed on all time scales. However, anticorrelations between variability amplitude and black hole mass estimate are evident on only the shortest time scales probed. The data are consistent with the models of power spectral density (PSD) movement described in Markowitz et al. (2003) and McHardy et al. (2004), whereby Seyfert 1 galaxies' variability can be described by a single, universal PSD shape whose cutoff frequency scales with black hole mass. The best-fitting scaling relations between variability time scale, black hole mass and X-ray luminosity support an average accretion rate of 2% of the Eddington limit for the sample. Nearly all sources exhibit stronger variability in the relatively soft 2–4 keV band compared to the 7–12 keV band on all time scales. Color-flux diagrams support also Seyfert 1s' softening as they brighten. There are indications that relatively less luminous or less massive sources exhibit a greater degree of spectral variability for a given increase in overall flux.

Subject headings: galaxies: active — galaxies: Seyfert — X-rays: galaxies

1. INTRODUCTION

X-ray observations can provide constraints on the physical conditions in the innermost regions of Seyfert 1 Active Galactic Nuclei (AGNs), as the X-rays are generally thought to originate in close proximity to the putative central supermassive black hole. On the basis of spectroscopic observations, the leading models of the X-ray continuum production include a hot, Comptonizing electron or electron-positron pair corona above and below an accretion disk. The corona multiply-upscatters thermal soft photons emitted from the disk to produce an X-ray power-law in the energy range 1–100 keV (e.g., Haardt, Maraschi & Ghisellini 1994). Furthermore, the disk, or some other cold, optically thick material, reprocesses the hard X-rays, as evidenced by the so-called 'Compton reflection humps' above ∼10 keV in Seyfert spectra, as well as strong iron fluorescent lines at ∼6.4 keV (Lightman & White 1988, Guilbert & Rees 1988, Pounds et al. 1990).

Seyfert 1 galaxies exhibit rapid, aperiodic X-ray continuum variability for which no fully satisying explanation has been advanced. Probably the best way to characterize single-band AGN variability, if adequate data exist, is to measure the fluctuation power spectral density (PSD) function. Recent studies such as Edelson & Nandra (1999), Uttley, McHardy & Papadakis (2002), Markowitz et al. (2003), Marshall et al. (2004) and McHardy et al. (2004) measured high-dynamic range broadband PSDs which showed the red-noise nature of Seyfert variability at high frequencies, but flattened below temporal frequencies corresponding to time scales of a few days. Markowitz et al. (2003) developed a scenario in which all Seyfert 1s have a PSD shape similar to that of XRBs and which scale towards lower temporal frequency with increasing black hole mass. Physically, this is consistent with a scenario in which relatively more massive black holes host larger X-ray emitting regions, the variability mechanism takes a longer time to propagate through the emission region, and the observed variability is 'slower.'

When data are not adequate to construct a PSD, it is still valuable to quantify the variability amplitude. The well-known anticorrelation between variability amplitude (as quantified over a fixed temporal frequency range) and source luminosity on both short time scales (∼1 d: Barr & Mushotzky 1986; Nandra et al. 1997, Turner et al. 1999) as well as long time scales (∼300 d: Markowitz & Edelson 2001, hereafter ME01) is consistent with the above physical interpretation.

Numerous X-ray spectral variability studies (e.g., Markowitz, Edelson & Vaughan 2003; also Nandra et al. 1997, ME01) have shown the majority of Seyferts to soften as they brighten, with the relatively softer energies displaying stronger variability. It is currently unclear whether this is due to instrinsic slope changes of the coronal power-law continuum or due to the presence of a much less variable hard component that is likely associated with the Compton reflection hump (e.g. Shih, Iwasawa & Fabian 2002; Taylor, Uttley & McHardy 2003). In contrast to the 'normal' or 'broad-line' Seyfert 1's which show this property, however, some 'narrow-line' or 'soft-spectrum' Seyfert 1s (characterized by FWHM < 2000 km s^{-1}, and steep pho-

ton indices; e.g., Boller, Brandt & Fink 1996) display spectral variability that is independent of energy (Edelson et al. 2002, Vaughan et al. 2002). This behavior is possible if the hard component mentioned above is absent or extremely weak in these objects.

The archival data accumulated by the *Rossi X-ray Timing Explorer* (*RXTE*) during its first seven years of operation permits a study of broadband continuum and spectral variability behavior on time scales ranging from days to years. The long-term variability survey of ME01 was the first to systematically probe X-ray variability on such long time scales, examining nine Seyfert 1 light curves each of 300 days in duration. This paper expands that survey to cover additional time scales and sources using additional archival *RXTE* data. In this paper we test the relation between X-ray variability and black hole mass, including the idea of broadband PSD movement with black hole mass, and exploring spectral variability throughout Seyfert 1s. The source selection and data reduction are described in §2. The sampling and analysis are described in §3. The results are discussed in §4, and a short summary is given in §5.

2. DATA COLLECTION AND REDUCTION

RXTE has observed ~55 Seyfert 1 galaxies during the first seven years of its mission. Data taken through most of Cycle 7 had turned public by 2004 February, when these analyses were performed. This paper considered these data as well as the authors' proprietary observations of three Seyfert 1 galaxies observed during Cycle 8. §2.1 details how the *RXTE* data were reduced.

The observational approach of this project was to obtain monitoring on multiple long time scales, sampled as uniformly as possible for as many Seyfert 1 galaxies as possible. Using the available archive of *RXTE* data to optimize this trade-off yielded a sample of 27 Seyfert 1s suitable for analysis on at least one of the time scales of interest, 1 d, 6 d, 36 d, 216 d, or 1296 d. Additionally, most of these sources also had adequate short time scale (1 d) *ASCA* data publically available. Most of the sources with data on the 36 d, 216 d, and 1296 d time scales have had their PSDs measured or are currently undergoing monitoring for future PSD measurement. §2.2 and §2.3 detail construction of the *RXTE* and *ASCA* light curves, respectively.

2.1. *RXTE data reduction*

All of the *RXTE* data were taken with the Proportional Counter Array (PCA), which consists of five identical collimated proportional counter units (PCUs; Swank 1998). For simplicity, data were collected only from those PCUs which did not suffer from repeated breakdown during on-source time (PCUs 0, 1, and 2 prior to 1998 December 23; PCUs 0 and 2 from 1998 December 23 until 2000 May 12; PCU 2 only after 2000 May 12). Count rates quoted in this paper are normalized to 1 PCU. Only PCA STANDARD-2 data were considered. The data were reduced using standard extraction methods and FTOOLS V5.2 software. Data were rejected if they were gathered less than 10° from the Earth's limb, if they were obtained within 30 min after the satellite's passage through the South Atlantic Anomaly (SAA), if ELECTRON0 > 0.1 (ELECTRON2 after 2000 May 12), or if the satellite's pointing offset was greater than 0.°02.

As the PCA has no simultaneous background monitoring capability, background data were estimated by using PCABACKEST V2.1E to generate model files based on the particle-induced background, SAA activity, and the diffuse X-ray background. This background subtraction is the dominant source of systematic error in *RXTE* AGN monitoring data (e.g., Edelson & Nandra 1999). Counts were extracted only from the topmost PCU layer to maximize the signal-to-noise ratio. All of the targets were faint (< 40 ct s^{-1} PCU^{-1}), so the applicable 'L7-240' background models were used. Because the PCU gain settings changed three times since launch, the count rates were rescaled to a common gain epoch (gain epoch 3) by calibrating with several public archive Cas A and Crab observations. Light curves binned to 16 s were generated for all targets over the 2–12 keV bandpass, where the PCA is most sensitive and the systematic errors and background are best quantified. Light curves were also generated for the 2–4 and 7–12 keV subbands. The data were binned on the orbital time scale; orbits with less than ten 16-second bins were rejected. Errors on each point were obtained from the standard deviations of the data in each orbital bin. Further details of *RXTE* data reduction can be found in e.g., Edelson & Nandra (1999).

2.2. *RXTE sampling*

The observational approach of this project was to quantify the continuum variability properties of Seyfert 1 galaxies on multiple time scales. This required assembling samples that were, to the greatest degree possible, uniformly monitored for proper comparison between sources. Sources with a weighted mean count rate significantly below 1 ct s^{-1} PCU^{-1} over the full 2–12 keV bandpass were rejected to minimize the risk of contamination from faint sources in the field-of-view and to ensure adequate signal-to-noise.

The sampling of the publically available data was highly uneven in general. The original observations were made with a wide variety of science goals, leading to a variety of sampling patterns and durations. This required us to clip light curves to common durations and resample at similar rates in order to produce samples with homogeneous sampling characteristics. For each total light curve, optimum windows of 1 d, 6 d, 36 d, 216 d, and 1296 d (evenly-spaced in the logarithm by a factor of 6) were selected. Given the original sampling patterns, these windows represented a reasonable spread in temporal frequency coverage, and yielded a reasonably-sized sample on each time scale. For each time scale, light curves shorter than the optimum window were rejected. Light curves with long gaps (>1/3 of the total duration) within the window were also rejected. Such gaps reduce the statistical significance of parameters derived over the full duration, and interpolating across such large gaps would result in an underestimate of the true variability amplitude. For each source, as many usable light curves as possible on each of the five time scales were selected from the total light curves. In NGC 3227, there was a significant hardening of the spectrum during approximately MJD 51900–52000, consistent with a temporary increase in cold absorption due to a dense cloud

passing along the line of sight (Lamer, Uttley & McHardy 2003); these data were excluded.

To extract light curves that were sampled as uniformly as possible, the light curves were resampled on each of the five time scales with a common, optimized rate. This was done using an algorithm that kept spaces between adjacent points as close to a rate $\Delta T_{\rm samp}$ as possible, where $\Delta T_{\rm samp}$ was 5760 sec (1 satellite orbit), 0.27 d (4 satellite orbits), 1.6 d, 5.3 d and 34.4 d for the 1, 6, 36, 216, and 1296 d light curves, respectively. Resampling at rates longer than $\Delta T_{\rm samp}$ would have resulted in too few points in each final light curve, while resampling at significantly more frequent rates would have resulted in light curves that were not sufficiently uniform, given the original range of observing patterns. The final light curves were also required to contain at least ~20 points (~15 on the 1 d time scale) in order to obtain an accurate estimate of the variability amplitude as quantified below; those light curves with fewer points were discarded. Light curves with poor signal to noise (i.e., due to mean count rates significantly less than 1.0) were discarded. Given that many sources were observed with overlapping sampling patterns, the final light curves for a given source often share data points on multiple time scales and are not completely independent.

This reduction yielded a total of 27 sources with sampling on each at least one of the five *RXTE* time scales. This included 86 observations of 18 sources on the 1 d time scale, 68 observations of 12 sources on the 6 d time scale, 19 observations of 12 sources on the 36 d time scale, 78 observations of 19 sources on the 216 d time scale, and 12 observations of 9 sources on the 1296 d time scale. Figure 1 shows the full 2–12 keV *RXTE* light curves for all 27 sources, before resampling, and showing the boundaries of the sampling windows. For clarity, some portions of light curves where there was no usable data (i.e., no adequate monitoring on the time scales of interest) are not shown. Table 1 lists source observation and sampling parmeters. All source luminosities were calculated using the global mean *RXTE* count rate and using the HEASARC's online WebPIMMS v.3.4 flux converter assuming an intrinsic power-law with a photon index obtained from either previously published spectral fits (e.g., Kaspi et al. 2001, Pounds et al. 2003) or the online Tartarus database of *ASCA* AGN observations (e.g., Nandra et al. 1997; Turner et al. 1999). Luminosities were calculated assuming $H_o = 70$ km s^{-1} Mpc^{-1} and $q_o = 0.5$.

2.3. *ASCA data*

Short-term *ASCA* 2–10 keV light curves were obtained from the Tartarus database for the sources with *RXTE* data. The count rates in the light curves provided had been combined and averaged between *ASCA*'s two Solid-state Imaging Spectrometers (SIS; Burke et al. 1994, Gendreau 1995) and binned to 16 s. For each source, all available light curves longer than 1 d in duration were selected from the database; otherwise the longest light curve >60 ksec in duration was used. The light curves were binned on orbital time scales, yielding 51 light curves of 11–15 consecutive orbital bins for 21 sources. Background light curves were similarly binned and subtracted to produce net count rate light curves. Table 2 lists source observation and sampling parameters for the *ASCA* data.

3. ANALYSIS

3.1. *Quantifying variability amplitudes*

Fractional variability amplitudes (F_{var}; e.g., Vaughan et al. 2003, Edelson et al. 2002) were measured for each light curve to quantify the instrinsic variability amplitude relative to the mean count rate and in excess of the measurement noise;

$$F_{var} = \sqrt{\frac{S^2 - \langle \sigma_{err}^2 \rangle}{\langle X \rangle^2}}, \quad (1)$$

where S^2 is the total variance of the light curve, $\langle \sigma_{err}^2 \rangle$ is the mean error squared and $\langle X \rangle$ is the mean count rate of N total points. The error on F_{var} is

$$\sigma_{F_{var}} = \sqrt{\left\{ \sqrt{\frac{\langle \sigma_{err}^2 \rangle}{N}} \cdot \frac{1}{\langle X \rangle} \right\}^2 + \left\{ \sqrt{\frac{1}{2N}} \cdot \frac{\langle \sigma_{err}^2 \rangle}{\langle X \rangle^2 F_{var}} \right\}^2} \quad (2)$$

as discussed in Vaughan et al. (2003); this error formulation estimates $\sigma_{F_{var}}$ based on random errors in the data itself, and not due to random variations associated with red-noise processes.

For multiple light curves for a given source and time scale, the values of F_{var} were averaged. In accordance with the linear RMS–flux relation seen in XRBs (Uttley & McHardy 2001) and Seyfert 1s (Edelson et al. 2002, Vaughan, Fabian & Nandra 2003), Seyfert 1 light curves are expected to reflect the "weakly stationary" behavior of the underlying variability process. That is, F_{var} is expected to be independent of flux level. However, in any red-noise stochastic process there will be random scatter in independent estimates of the variance due to statistical fluctuations; such scatter is not necessarily indicative of non-stationary behavior. One needs at least 10–20 independent estimates of F_{var} to adequately test if those estimates are consistent with their average value $\langle F_{var} \rangle$ (see Vaughan et al. 2003 for detailed descriptions of such tests). There are only three objects with enough data for this relatively strong test, NGC 7469, IRAS 18325–5926 and MCG–6-30-15 on the 1 d time scales (with the *RXTE* 2–12 keV and *ASCA* 2–10 keV values considered together); in all three cases at least 70% of the individual values of F_{var} are consistent with $\langle F_{var} \rangle$. For the rest of the sample, when multiple estimates of F_{var} were made, the measured values were usually reasonably close to $\langle F_{var} \rangle$. This is consistent with weakly stationary behavior. Thus, these values of $\langle F_{var} \rangle$ are used hereafter. Table 3 lists the fractional variability amplitudes for each *RXTE* light curve over the 2–12 keV, 2–4 keV and 7–12 keV bands. Table 4 lists the fractional variability amplitudes over the 2–10 keV band for the *ASCA* data.

3.2. *Construction of correlation diagrams*

Figures 2 and 3 display the values of F_{var} plotted against 2–12 keV luminosity L_{2-12} and black hole mass estimate $M_{\rm BH}$ (e.g., reverberation mapped mass estimates from Kaspi et al. 2000), respectively. The *ASCA* data are included and agree well with the 1-d *RXTE* data; one should not expect any significant difference between parameters derived over the 2–10 and 2–12 keV bands. The slopes of the best-fitting logarithmic power law for each data set

are listed in Table 5; the Pearson correlation coefficients r and probability P_r of obtaining those values of r by chance are also listed in Table 5. As seen in Figure 2, all six data sets conform well to power laws of the form $F_{var} \propto L_{2-12}^{-a}$ at greater than 95% significance. Such anticorrelations have been observed previously in AGNs for ~1 d time scales (Green, McHardy & Lehto 1993, Nandra et al. 1997). However, the slopes and normalizations of the best-fitting logarithmic power law for each data set differ: the slopes generally flatten towards longer time scales. The 1-d and 216-d time scale relations are generally consistent with the 1 d and 300 d relations of ME01.

As seen in Figure 3, however, not all data sets conform well to power laws of the form $F_{var} \propto M_{BH}^{-a}$ overall. Both 1-d data sets are well correlated at >99.8% significance. The 6-d data set is moderately well correlated, at 96.7% significance. However, due to large scatter, strong or significant anticorrelations are not evident for two of the three longest time scales, 36-d and 1296-d. The 216-d data set, which is generally consistent with the 300-d time scale relation in Papadakis (2004), is found to be moderately correlated ($r = 0.50$) at >97% significance. The data sets have been fitted by logarithmic power law slopes that also generally flatten towards longer time scales, as listed in Table 5. For all objects, the values of F_{var} generally increase towards longer time scales, levelling off somewhat beyond approximately the 36 d time scale relation, but the highest mass and highest luminosity sources show the largest increase.

It can be seen from the values of F_{var} listed in Table 3 that most observations (56/68) show stronger variability in the 2–4 keV band compared to the 7–12 keV band. Formally, the null hypothesis of the 2–4 keV and 7–12 keV excess variances (square of the F_{var}) being consistent is rejected using an F-test at >90% significance in 12 observations and >95% significance in 8 observations. The zero-lag correlation diagram for 2–4 keV F_{var} versus 7–12 keV F_{var}, for all five *RXTE* data sets, is shown in Figure 4. It can be seen that the vast majority of points lie to the right of the dashed line which represents equal variability in the two bands. This shows again that most sources exhibit stronger variability in the relatively softer band. On all time scales, the data conform very well to power-laws at >99.99% significance; slopes and values of r and P_r are listed in Table 5. There is no obvious indication that the degree of spectral variability exhibited is dependent on the time scale probed.

Figure 5 shows the ratio of 2–4 keV F_{var} / 7–12 keV F_{var} plotted against L_{2-12} for all five *RXTE* data sets. The slopes and values of r and P_r are listed in Table 5. Also listed in Table 5 are the ratios of 2–4 keV F_{var} / 7–12 keV F_{var} versus M_{BH} (not plotted). There is considerable scatter in all data sets, and there are no correlations significant at >99%. The best-fitting slopes are all similar; the slopes might be taken as tentative evidence for relatively less luminous or less massive sources to be more strongly variable in the soft band. Again, there is no obvious indication that the degree of spectral variability exhibited is dependent on the time scale probed.

Color-flux diagrams, in the which the logarithm of the 7–12 keV / 2–4 keV count rate hardness ratio (HR) is plotted against the logarithm of the geometric mean of the the count rates in these two bands, are shown in Figure 6. To minimize the effects of changes in spectral response due to PCA gain epoch changes, only the largest number of points within a single gain epoch was used for each source. Light curves of ~300 days in duration, with no resampling, were used; light curves with less than 70 points were discarded. This yielded a sample of 27 light curves for 15 sources; date ranges are listed in Table 6. For each source, the data were sorted by increasing geometric mean and grouped into bins of 16 points; the highest flux bin was ignored if it contained less than 10 points. For most sources, the data form a continuous, well-defined region. It is clear from these diagrams as well that nearly all sources soften as they brighten. The two expections, which show either a slight hardening or no spectral variability with flux, are the NLSy1 Ark 564 and the radio-quiet quasar PG 0804+761, as has been reported previously (Edelson et al. 2002; Papadakis, Reig & Nandra 2003). Also shown in Figure 6 is the best fitting linear fit to the binned data. Table 6 lists the mean hardness ratio values ⟨HR⟩ for each source. For the sample as a whole, the average of the 27 mean hardness ratios is ~1.06. While 10 sources' ⟨HR⟩ values are within 20% of the sample average, two sources are notably softer (PG 0804+761 and Ark 564) and three are notably harder (NGC 3516, NGC 4151 and NGC 3227).

Also listed in Table 6 is a parameter derived directly from the slope m of the best linear fit, $\phi = 2.0^{-m}$, which quantifies the decrease in HR for every doubling in geometric mean count rate. Multiply-measured values of ⟨HR⟩ and ϕ for a given object tend to be consistent with each other, suggesting that sources do not undergo any radical changes in spectral variability behavior over times scales of one or two years. ϕ is greater than 1 for all sources except PG 0804+761 and Ark 564. It is noted that these two sources have the lowest 7–12 keV mean count rates in the sample (less than 0.4 c/s/PCU); it is conceivable that systematic variations in the modelled background may contribute greatly to the observed 7–12 keV variability at such low flux levels. The *RXTE* data for PG 0804+761 and Ark 564 will therefore not be considered further here.

Figure 7 shows ϕ plotted against L_{2-12} and M_{BH}. There are strong anticorrelations between ϕ and L_{2-12} ($r = -0.692$, $P_r = 8.77\times10^{-3}$ for 13 sources) and between ϕ and M_{BH} ($r = -0.673$, $P_r = 1.17\times10^{-2}$ for 13 sources). These diagrams indicate that relatively less luminous or less massive sources display a stronger degree of spectral variability per given increase in overall flux.

It is noted that other studies (Edelson et al. 2002; Papadakis, Reig & Nandra 2004) have found Ark 564 and PG 0804+761 to show hardness ratios that are independent of flux, which would imply values of ϕ near 1. It is noted that both sources would thus lie reasonably close to the observed ϕ–L_{2-12} anticorrelation. Additionally, the high-mass PG 0804+761 would lie close to the ϕ–M_{BH} anticorrelation; however, Ark 564 would be a significant outlier if added to the ϕ–M_{BH} anticorrelation.

4. DISCUSSION

When one uses the fractional variability, F_{var}, as a description of the intrinsic, underlying variability process, certain caveats must be kept in mind when red-noise processes are relevant. Each light curve is an independent realization of the underlying stochastic process and there will

be random fluctuations in the measured variance. However, in the absence of evidence for strongly non-stationary behavior in Seyfert light curves (e.g., §3.1, Markowitz et al. 2003, Vaughan et al. 2003), it is assumed hereafter that the values of F_{var} are reasonable quantifications of the intrinsic variability amplitude. The reader must keep in mind the previously discussed limitations when considering such small numbers of F_{var} estimates.

The anticorrelation between variability amplitude and source luminosity seen in previous surveys is confirmed here on all five time scales probed. There is a strong anticorrelation between $M_{\rm BH}$ and F_{var} on time scales of 1 day; this has been seen before by Nikolajuk et al. (2004). There is a moderately strong anticorrelation on the 6-d time scale; however, the $M_{\rm BH}$–F_{var} relation cannot be confirmed for time scales of 36 days or longer. In both sets of anticorrelations, the best-fitting power-law slopes gradually decrease towards longer time scales. The F_{var} values tend to increase towards longer time scales, however, they tend to saturate beyond the 36 d time scale. Consequently, the increase in F_{var} is greatest for the higher luminosity sources. As explained in §4.1, this trend is consistent with a scaling of PSD turnover frequency with some fundamental parameter, most likely $M_{\rm BH}$. All of the sources exhibit stronger variability towards relatively softer energies. Additionally, sub-band F_{var} values and color–flux diagrams indicate that less luminous sources have a tendency to exhibit more spectral variability overall. These spectral variability characteristics are discussed in the context of simple X-ray reprocessing models in §4.2.

4.1. *The variability–luminosity–$M_{\rm BH}$ relationship*

Recent PSD studies have yielded PSD cutoffs on time scales of a few days or less; in most cases, the power-law slopes flatten from ∼–2 above the break to ∼–1 below the break. There are not enough adequate data to construct high dynamic range PSDs for all targets in the current sample. However, it is reasonable to assume that all Seyferts have similar PSD shapes with cutoffs. Given the ranges of luminosity and black hole masses spanned by the sample, it is reasonable to assume that the longest time scales probes in this survey are exploring variability on temporal frequencies well below the cutoffs in most or all of the sources. This would then explain why the variability amplitudes observed tend to saturate at similar levels on the longest time scales probed, strongly reducing the dependence of F_{var} on $M_{\rm BH}$ or luminosity. However, the data are not able to highly constrain if objects' PSDs contain a second, low-frequency break, due to the saturation of F_{var}.

Markowitz et al. (2003) developed a picture in which all Seyfert 1 PSDs have the same shape but whose high-frequency break time scales $T_{\rm b}$ scale linearly in temporal frequency with $M_{\rm BH}$. This is consistent with observed anticorrelations between F_{var} and $M_{\rm BH}$ (Papadakis 2004, O'Neill et al. 2004) and F_{var} and X-ray luminosity (e.g., Nikolajuk et al. 2004). Interestingly, though, the PSD break frequencies appeared to be less correlated with bolometric luminosity $L_{\rm bol}$. Using the values of F_{var} measured here, it is possible to further test this picture. F_{var} for any given object depends on the detailed PSD shape: specifically, it depends on the presence or lack of a break as well as the PSD normalization A. The accumulation of Seyfert PSDs supports a wide spread in observed values of A (e.g., Uttley et al., in prep.); the wide spread in F_{var} on the longest time scales supports this notion. To remove the dependence of the $T_{\rm b}$–$M_{\rm BH}$ and $T_{\rm b}$–L_{2-12} relations on A, the ratios R_{Fvar} of measured values of 2–12 keV F_{var} on six combinations of time scales (1 d/6 d, 1 d/36 d, 1 d/216 d, 1 d/1296 d, 6 d/216 d and 6 d/1296 d) are considered; these six ratios predict the biggest range in F_{var} across the ranges of $M_{\rm BH}$ and L_{2-12} sampled. Values of F_{var} on the 1 d time scale were combined between the *ASCA* and *RXTE* data sets. Figures 8 and 9 show the measured F_{var} ratios plotted as a function of $M_{\rm BH}$ and L_{2-12}, respectively. The solid lines show best-fit model F_{var} ratios derived from a simple linear PSD scaling in frequency. It was assumed that all Seyferts have the same singly-broken PSD shape $P(f)$, described by $P(f) = A(f/f_b)^{-1}$ (for $f < f_b$), or $P(f) = A(f/f_b)^{-2}$ (for $f > f_b$). A is the PSD normalization at the high-frequency break f_b, calculated as 0.01 $({\rm Hz}^{-1})/f_b$, a relation estimated from the A–$M_{\rm BH}$ and $T_{\rm b}$–$M_{\rm BH}$ plots of Markowitz et al. (2003; their figures 12 and 13). The PSDs assumed a linear scaling in frequency for both plots. The F_{var} values were calculated by integrating the PSD between the temporal frequencies of $1/D$ (where D is 1, 6, 36, 216, or 1296 days) and $1/2\Delta T_{\rm samp}$. Power contribution from aliasing was estimated by integrating the model PSD from the Nyquist frequency to a frequency of 1/(2000 s). Power contribution from red-noise leak was added, estimated by using Monte Carlo simulations to determine the red-noise leak contribution from variations on time scales of D to $50D$. No arbitrary scaling in the y-direction of the resulting values of R_{Fvar} was done. The predicted R_{Fvar} functions were best-fit in the x-direction and are plotted in both Figures 8 and 9. The fits indicate that the linear PSD scaling for Figure 8 requires the relation $T_{\rm b}$ (days) = $M_{\rm BH}/10^{7.05}\,{\rm M}_\odot$. For Figure 9, the linear PSD scaling required is $T_{\rm b}$ (days) = $L_{2-12}/$ ($10^{43.35}$ erg s^{-1}). These two relations suggest the average accretion rate for the entire sample is ∼2% of the Eddington limit.

McHardy et al. (2004) suggested that the normalization of a linear $T_{\rm b}$–$M_{\rm BH}$ relation may be dependent on some other parameter, possibly the accretion rate. Under the assumption that the reverberation masses are accurate, the picture emerging from PSD measurement seems to be revealing a bifurcation in Seyfert PSDs. It appears that some Seyferts' PSD cutoffs lie close to a $T_{\rm b}$–$M_{\rm BH}$ scaling that is approximately quantified as $T_{\rm b}$ (days) = $M_{\rm BH}/10^{6.5}\,{\rm M}_\odot$ (e.g., NGC 3516, NGC 4151, and NGC 3783; Markowitz et al. 2003). This relation extrapolates 6–7 orders of magnitude to the PSD cutoff of Cyg X-1 in the low/hard state. Other sources (NGC 4051 and possibly other narrow-line Seyfert 1s; McHardy et al. 2004) seem to require a $T_{\rm b}$–$M_{\rm BH}$ scaling that is approximately $T_{\rm b}$ (days) = $M_{\rm BH}/10^{7.5}\,{\rm M}_\odot$. This relation extrapolates to the the PSD cutoff of Cyg X-1 in the high/soft state, arguing some connections between these Seyfert s XRBs in the high/soft state. The best-fitting linear $T_{\rm b}$–$M_{\rm BH}$ relation derived from the present sample lies in between these two scalings; this is consistent with the idea that the present sample contains a mixture of sources from the two groups.

The values of R_{Fvar} can further support the notion that PSD scaling is more strongly dependent on $M_{\rm BH}$ than on

luminosity. For each ratio, the predicted and model R_{Fvar} values were compared in a χ^2 sense for all ten combinations of time scales. For eight of the ten ratios (all except the 36 d/1296 d and 216 d/1296 d ratios), the values of χ^2 are lower in the R_{Fvar}–$M_{\rm BH}$ diagram compared to those in the R_{Fvar}–L_{2-12} diagram, typically by a factor of ~2.0 (For the 36 d/1296 d and 216 d/1296 d ratios, the values of χ^2 in the R_{Fvar}–L_{2-12} plot are 0.94 and 0.95, respectively, those in the R_{Fvar}–$M_{\rm BH}$ plot.). Overall, the measured values of R_{Fvar} cannot definitively distinguish between a linear scaling of PSD time scale in luminosity versus a scaling with $M_{\rm BH}$, but $M_{\rm BH}$ appears to be preferred.

Another possibility is that the reverberation-mapped mass estimates used, while reliable to first order, may not be reliable to the highest degree expected. We cannot rule out the possibility that some of the mass estimates used herein may possibly require some refinement via additional reverberation-mapping analysis. However, this is unlikely; reverberation and stellar velocity dispersion methods generally give consistent results to within a factor of a few (Woo & Urry 2002). Additionally, recent reverberation-mapping campaigns for a few targets yield black hole masses consistent with older, initial estiamtes (e.g., Onken & Peterson 2002; Onken et al. 2003).

4.2. *Spectral variability*

The majority of the Seyferts sampled show stronger variaiblity towards softer energies, as seen from a comparison of the 2–4 keV and 7–12 keV F_{var} values, and from the color-flux diagrams. Such behavior is consistent with the well-documented property of Seyfert 1s to soften as they brighten. Some works have suggested spectral pivoting of the coronal power law about some energy above 10 keV as the explanation for Seyferts' softening as they brighten (e.g., Papadakis et al. 2002). Thermal Comptonization models predict changes in the intrinsic spectral slope of the coronal component, Γ_{int}. In such a scenario, the corona's luminosity remains constant while the seed photon flux varies, affecting the corona's temperature. Spectral pivoting can also arise if the corona is dominated by electron-positron pairs (Haardt, Maraschi & Ghisellini 1997). However, spectral variability studies by McHardy, Papadakis & Uttley (1998), Shih et al. (2002) and Lamer et al. (2003) have shown that the spectral fit photon index saturates at high flux. To explain this effect, McHardy, Papadakis & Uttley (1998) and Shih et al. (2002) independently proposed the "two-component" model consisting of a constant hard reflection component superimposed upon a soft coronal component that is variable in normalization but constant in spectral shape. That is, Γ_{int} is constant due to both the disk seed and coronal fluxes increasing.

Tools such as the color-flux plots, or e.g., the flux-flux plots in Taylor, Uttley & McHardy (2003) offer a potential way to distinguish between these two types of spectral variability, though, as shown below, the quality of the current data set hinders the ability to distinguish between spectral pivoting at high energies, e.g., $\gtrsim$3000 keV, and the two-component, constant-Γ_{int} spectral variability.

The color-flux diagrams not only show that Seyfert 1s generally soften as they brighten, they also tentatively suggest that there is more spectral variability for a given increase in flux for the relatively less luminous, less massive, and more variable overall sources. Additional support comes from the marginal anticorrelations between the ratios of the 2–4 keV and 7–12 keV F_{var} and luminosity (Figure 5) and $M_{\rm BH}$. This trend could be due to the presence of some variable soft component present in the 2–4 keV band but not evident at higher energies; this component could be more prominent or more variable in the relatively lower luminosity objects. Alternatively, the physical parameters which ultimately constrain the amount of observed spectral variability may themselves be more variable in the relatively lower luminosity objects. Another possible contribution to this effect may possibly arise from the energy-dependency of the high-frequency PSD (e.g., Papadakis & Nandra 2001, Vaughan, Fabian & Nandra 2003, McHardy et al. 2004). At temporal frequencies above the break, PSD slopes tend to increase in slope as photon energy increases, typically by ~0.1–0.2 for a doubling in photon energy. One would then observe a reduction in the ratio of soft to hard X-ray variability in more massive or luminous sources, since their PSD breaks appear at relatively lower temporal frequencies. However, simulations show that such an effect is minor. Simulations of 300-day light curves using PSD shapes with energy-dependent high-frequency slopes (change in slope by 0.2 between the two bands), energy-dependent normalization A (roughly 50% higher in the soft band; e.g., McHardy et al. 2004), and a T_b–$M_{\rm BH}$ relation as per above yield a reduction in the ratio of soft to hard F_{var} by ~6% over the $M_{\rm BH}$ range of interest. This corresponds to a change in ϕ of only ~7%, much smaller than the range observed.

4.2.1. *Models of spectral variability*

The color-flux diagrams are compared to models of the two types of spectral variability as generated by XSPEC v. 11 (Arnaud 1996) as a crude, but independent estimate of spectral parameters. A grid of spectral pivoting models with Γ_{int} spanning 1.2, 1.3, ... ,2.8 was generated by using the FAKEIT command to simulate spectra folded through the appropriate *RXTE* response matrix for each gain epoch. The basic model was a power law plus a 6.4 keV narrow (width of 0.15 keV) Gaussian plus a Compton reflection hump modelled with PEXRAV (Magzdziarz & Zdziarski 1995), all modified by neutral absorption fixed at 3×10^{20} cm^{-2}. The line's normalization was fixed at 1/100 the power law normalization A_Γ to simulate a fixed equivalent width. Pivot energies at 30, 100, 300, 1000 and 3000 keV were considered. Relative reflection values R (ratio of the reflection normalization A_R to that of A_Γ) of 0, 1 and 2 were considered. 2–4 keV and 7–12 keV fluxes and their geometric means and hardness ratios were calculated and compared with the measured hardness ratios and values of ϕ. Multiply-measured values of HR and ϕ were averaged. All models can be stretched to be consistent with the data; the comparisons between modelled and observed hardness ratios and ϕ are only approximate. PG 0804+761 and Ark 564 are included with ϕ=1 assumed; strictly speaking, this requires an infinite pivot energy.

Spectral pivoting at 30 keV leads to a decrease in the hardness ratio by ~1.7 for every doubling in geometric mean count rate (the ϕ parameter introduced earlier), with the corresponding increase in photon index, $\Delta\Gamma_2$, of ~0.4–

0.5. These values are approximately constant over the whole modelled ranges of Γ_{int} tested. This predicted ϕ is somewhat larger than the values measured herein for all the sources, and spectral pivoting about 30 keV is therefore not an optimum model. Spectral pivoting at higher energies (100, 300, 1000 and 3000 keV) yields progressively smaller values of ϕ ($\sim$1.3, $\sim$1.25, $\sim$1.2, and $\sim$1.1, respectively) and $\Delta\Gamma_2$ ($\sim$0.3–0.4, $\sim$0.2, $\sim$0.1–0.2, and $\sim$0.1). We note that these latter models of pivot energies yield predictions similar to that of Haardt, Maraschi & Ghisellini (1997) for a pair-dominated corona, wherein an increase in 2–10 keV flux (which corresponds to an increase in the geometric mean of the 2–4 keV and 7–12 keV count rates by a factor of 6), corresponds to an increase in Γ_{int} by 0.2. However, the current data cannot adequately constrain the pivot energy. Table 7 lists the most plausible model parameter combinations for each source based solely on the information obtained from the color-flux diagrams in Table 6. We stress that this is only approximate and that the parameters listed are not highly constraining; i.e., pivot energy is likely only good to within a factor of at least 30–100 and median Γ_{int} is likely only good within $\sim$0.4. However, there is reasonable consistency with many other published spectral fits and spectral variability studies (e.g., Papadakis et al. 2002; Gliozzi, Sambruna & Eracleous 2003; Lamer et al. 2003; Markowitz, Edelson & Vaughan 2003).

Spectral variability based on the two-component model, where Γ_{int} remains fixed, was also modelled. Values of Γ_{int} spanning 1.2, 1.3, ..., 2.8 were modelled with A_R held fixed. For each Γ_{int}, values of A_Γ equal to $0.2\times(10.0^{0.0,0.2,...,2.0})\times A_R$ were modelled (allowing A_R/A_Γ to range from 0.05 to 5.0). This model of spectral variability predicts that the broadband spectral fit Γ, which is always flatter than Γ_{int} if there is a non-zero reflection component, saturates at high flux, typically below where A_R/A_Γ is $\sim$0.2. Sources with flat color-flux trends (such as PG 0804+761 and Ark 564) could conceivably represent some (small) portion of the saturation tail, though. As with the spectral pivoting models, the models can be stretched to accomodate the observations for all sources. Table 7 lists plausible approximate parameter combinations for the sources; the median Γ_{int} listed is likely only good to within $\sim$0.4, and the median $A_R/A_{\Gamma_{int}}$ is likely only good to within a factor of $\sim$3–10. Again, there is reasonable consistency with numerous previous spectral studies. For the two sources which do not display spectral softening with flux, PG 0804+761 and Ark 564, Γ_{int} was estimated assuming A_R/A_Γ set equal to zero (which yields ϕ=1).

At this stage it is only speculative to conclude that the color-flux diagrams definitively distinguish between the two types of spectral variability discussed above. Direct spectral fitting to data from a future mission with higher sensitivity $\gtrsim$10 keV or below 2 keV may help resolve this issue.

5. CONCLUSIONS

This paper extends the results of the first long-term X-ray variability survey of ME01 to additional sources and time scales, including sampling variability on time scales well below the putative PSD cutoffs in Seyferts. The well-studied luminosity–variability amplitude anticorrelation is confirmed on multiple time scales. The anticorrelation between black hole mass and variability amplitude is confirmed on time scales of 1 d, but not on the longest time scales probed. Variability amplitudes increase towards longer time scales, consistent with red-noise variability, but the relatively more luminous sources show the greatest increase. For both sets of anticorrelations, the best-fitting slopes decrease towards longer time scales. These trends are consistent with a simple scaling of PSD break frequency with black hole mass as suggested by Markowitz et al. (2003) and McHardy et al. (2004), with F_{var} saturating on time scales below the PSD breaks, and the best-fitting relation quantified as T_b (days) = $M_{BH}/10^{7.05}\,M_\odot$. The measurement of a larger number of Seyfert PSDs at low temporal frequencies and additional accumulation of F_{var} measurements on multiple time scales for a given object may resolve this issue by further defining the relations between PSD time scale, PSD normalization, F_{var}, black hole mass and luminosity; such an undertaking is one of the of the goals of *Lobster–ISS* mission starting in $\sim$2009[3].

Nearly all the observations show relatively stronger variability towards softer energies, as seen from the values of F_{var}. Color-flux diagrams additionally show that sources soften as they brighten. The color-flux diagrams also tentatively suggest that sources with relatively lower luminosities or black hole masses display a larger range of spectral variability for a given increase in total X-ray flux.

The authors acknowledge the dedication of the entire *RXTE* mission team. This work has made use of data obtained through the High Energy Astrophysics Science Archive Research Center Online Service, provided by the NASA Goddard Space Flight Center, the TARTARUS database, which is supported by Jane Turner and Kirpal Nandra under NASA grants NAG 5-7385 and NAG 5-7067, and the NASA/IPAC Extragalactic Database which is operated by the Jet Propulsion Laboratory, California Institute of Technology, under contract with the National Aeronautics and Space Administration.

REFERENCES

Arnaud, K. 1996, in *Astronomical Data Analysis Software and Systems*, Jacoby, G., Barnes, J., eds., ASP Conf. Series Vol. 101, p. 17
Barr, P., & Mushotzky, R. 1986, Nature, 320, 421
Bian, W. & Zhao, Y. 2003, MNRAS, 343, 164
Boller, Th., Brandt, W.N., Fink, H. 1996, A&A, 305, 53
Burke, B.E., Mountain, R.W., Daniels, P.J., & Dolat, V.S. 1994, IEEE Trans. Nuc. SCI. 41, p. 375
Edelson, R. & Nandra, K. 1999, ApJ, 514, 682
Edelson, R., Turner, J., Pounds, K., Vaughan, S., Markowitz, A., Marshall, H., Dobbie, P., Warwick, R. 2002, ApJ, 568, 610
Gendreau, K. 1995. Ph.D. thesis, Massachusetts Institute of Technology
Gliozzi, M., Sambruna, R., Eracleous, M. 2003, ApJ, 584, 176
Green, A., McHardy, I., & Lehto, H. 1993, MNRAS, 265, 664
Guilbert, P. & Rees, M. 1988, MNRAS, 233, 475

[3] See http://www.src.le.ac.uk/lobster

Haardt, F., Maraschi, L. & Ghisellini, G. 1994, ApJ, 432, L95
Haardt, F., Maraschi, L. & Ghisellini, G. 1997, ApJ, 476, 620
Kaspi, S., Smith, P., Netzer, H., Maoz, D., Jannuzi, B., & Giveon, U. 2000, ApJ, 533, 631
Kaspi, S., Brandt, W., Netzer, H., George, I., Chartas, G., Behar, E., Sambruna, R., Garmire, G., & Nousek, J. 2001, ApJ, 554, 216
Lamer, G., McHardy, I.M., Uttley, P. & Jahoda, K. 2003, MNRAS 338, 323
Lamer, G., Uttley, P. & McHardy, I.M. 2003, MNRAS, 342, L41
Lightman, A.P., & White, T.R. 1988, ApJ, 335, 57
Magdziarz, P., & Zdziarski, A., 1995, MNRAS, 273, 837
Markowitz, A. & Edelson, R. 2001, ApJ, 547, 684
Markowitz, A. et al. 2003, ApJ, 593, 96
Markowitz, A., Edelson, R. & Vaughan, S., ApJ, 598, 935
Marshall, K., Ferrara, E.C., Miller, H.R., Marscher, A.P. & Madejski, G. 2004, proceedings of "X-Ray Timing 2003: Rossi and Beyond," ed. P. Kaaret, F.K. Lamb, & J H. Swank (Melville, NY: American Institute of Physics) (astro-ph/0312422)
McHardy, I.M., Papadakis, I.E. & Uttley, P. 1998, Nucl. Phys. B (Proc. Suppl.), 69/1-3, 509
McHardy, I.M. et al. 2004, MNRAS, 348, 783
Nandra, K. et al. 1997, ApJ, 476, 70
Nikolajuk, M., Papadakis, I.E. & Czerny, B. 2004, MNRAS, submitted (astro-ph/0403326)
O'Neill, P.M., Nandra, K., Papadakis, I.E. & Turner, T.J. 2004, MNRAS, submitted (astro-ph/0403569)
Onken, C. & Peterson, B.M., 2002, ApJ, 572, 746
Onken, C.A., Peterson, B.M., Dietrich, M., Robinson, A. & Salamanca, I.M. 2003, ApJ, 585,121
Papadakis, I.E. & Nandra, P. 2001, ApJ, 554, 710
Papadakis, I.E., Petrucci, P.-O., Maraschi, L., McHardy, I.M., Uttley, P. & Haardt, F. 2002, ApJ, 573, 92
Papadakis, I.E., Reig, P. & Nandra, K. 2003, MNRAS, 344, 993
Papadakis, I.E. 2004, MNRAS, 348, 207
Pounds, K., Nandra, K., Stewart, G., George, I., & Fabian, A., 1990, Nature, 344, 132
Pounds, K.A., Reeves, J.N., Page, K.L., Edelson, R., Matt, G., Perola, G.C. 2003, MNRAS, 341, 953
Santos Lleo, M. et al. 2001, A&A, 369, 57
Shemmer, O., Uttley, P., Netzer, H. & McHardy, I.M. 2003, MNRAS, 343, 1341
Shih, D.C., Iwasawa, K. & Fabian, A.C. 2002, MNRAS, 333, 687
Swank, J. 1998, in Nuclear Phys. B (Proc. Suppl.): The Active X-ray Sky: Results From BeppoSAX and Rossi-XTE, Rome, Italy, 1997 October 21-24, eds. L. Scarsi, H. Bradt, P. Giommi, & F. Fiore, Nucl. Phys. B Suppl. Proc. (The Netherlands: Elsevier Science B.V.), 69, 12
Taylor, R., Uttley, P., McHardy, I. 2003, MNRAS, 342, L31
Turner, T.J., George, I.M., Nandra, K. & Turcan, D. 1999, ApJ, 524, 667
Uttley, P. & McHardy, I. 2001, MNRAS, 323, L26
Uttley, P., McHardy, I. & Papadakis, I.E. 2002, MNRAS, 332, 231
Vaughan, S., Boller, Th., Fabian, A.C., Ballantyne, D., Brandt, W. & Trumper, J. 2002, MNRAS, 337, 247
Vaughan, S., Fabian, A., Nandra, K. 2003, MNRAS, 339, 1237
Vaughan, S., Edelson, R., Warwick, R. & Uttley, P. 2003, MNRAS, 345, 1271
Wandel, A., Peterson, B.M. & Malkan, M. 1999, ApJ, 526, 579
Wandel, A., 2002, ApJ, 565, 762
Wang, T.G., Matsuoka, M., Kubo, H., Mihara, T. & Negoro, H. 2001, ApJ, 554, 233
Woo, J. & Urry, C.M. 2002, ApJ, 579, 530

TABLE 1
SOURCE AND *RXTE* SAMPLING PARAMETERS

Time Scale	Source Name	z	$\log(L_{2-12})$ (erg s^{-1})	$\log(M_{\rm BH})$ ($M_\odot$)	MJD Range	Num. Pts.	Mean c s^{-1}	Mean S/N
1 d	PKS 0558–504	0.137	44.90	7.7	50734.31–50735.24	14	1.29	48
	3C 111	0.049	44.63	—	50530.93–50531.66	11	4.36	102
					51982.37–51983.43	13	7.95	72
					51983.43–51984.49	12	7.94	76
	Mkn 509	0.034	44.33	9.2±1.1	52012.20–52013.26	15	6.09	75
	3C 120	0.033	44.24	$7.48^{+0.21}_{-0.28}$	52621.91–52622.90	12	5.47	69
					52622.90–52623.89	13	5.61	66
					52623.89–52624.88	13	5.98	79
					52624.88–52625.93	11	5.70	82
					52625.94–52626.99	11	5.29	87
					52628.31–52629.10	11	4.81	68
					52629.37–52630.35	12	6.54	83
					52678.12–52679.15	14	6.01	82
					52679.18–52681.22	14	5.73	73
	MCG–2-58-22	0.047	44.24	8.5	50797.97–50798.91	15	3.59	100
					51486.10–51487.10	12	3.19	69
	Ark 120	0.032	44.02	$8.27^{+0.09}_{-0.11}$	51163.37–51164.37	12	3.94	101
					51164.71–51165.51	13	3.83	106
	Mkn 279	0.030	43.82	7.4	52412.29–52413.21	14	1.40	18
	NGC 5548	0.017	43.63	$7.97^{+0.08}_{-0.07}$	50984.88–50985.88	14	9.00	183
					50985.89–50986.88	12	9.15	202
	Ark 564	0.025	43.62	6.1	50440.66–50441.66	15	2.21	53
	NGC 7469	0.016	43.38	$6.88^{+0.29}_{-6.88}$	50244.04–50245.04	15	3.18	66
					50245.04–50246.04	14	3.31	62
					50246.05–50247.04	15	2.75	57
					50247.05–50248.04	14	3.38	60
					50248.05–50249.05	15	3.48	57
					50249.05–50250.05	14	3.65	64
					50250.06–50251.05	13	3.41	54
					50251.06–50252.05	15	3.26	55
					50252.06–50253.06	13	2.38	48
					50253.06–50254.06	13	2.73	53
					50254.07–50255.06	13	3.09	53
					50255.07–50256.06	13	2.56	44
					50268.37–50269.36	11	3.42	58
					50269.44–50270.43	11	3.40	68
					50270.64–50271.58	11	3.03	67
					50271.64–50272.58	11	2.40	53
					50272.65–50273.58	13	2.74	55
					50273.65–50274.57	13	2.96	65
					50274.65–50275.65	14	3.08	68
	IRAS 18325-5926	0.020	43.36	—	50807.10–50808.09	15	1.67	47
					50808.10–50809.10	15	2.48	67
					50865.71–50866.70	15	1.80	58
					50866.70–50867.70	14	1.61	59
	NGC 3783	0.010	43.31	$6.94^{+0.05}_{-0.06}$	50112.73–50113.59	13	5.84	100
	Mkn 766	0.013	43.27	5.9	52036.02–52037.08	12	4.01	43
	NGC 4593	0.009	43.03	$6.82^{+0.25}_{-0.57}$	52089.03–52089.96	14	4.58	73
					52455.91–52456.96	12	5.18	60
	NGC 3516	0.009	43.00	$7.23^{+0.07}_{-0.10}$	50589.98–50590.97	15	4.40	143
					50590.98–50591.97	15	4.18	125
					50591.98–50592.98	15	4.40	145

TABLE 1—*Continued*

Time Scale	Source Name	z	$\log(L_{2-12})$ (erg s^{-1})	$\log(M_{BH})$ ($M_\odot$)	MJD Range	Num. Pts.	Mean c s^{-1}	Mean S/N
					50592.98–50593.98	15	3.91	136
					50916.30–50917.30	15	5.90	151
					50917.30–50918.30	15	5.74	141
					50918.31–50919.30	15	5.39	143
					52009.36–52010.35	15	3.23	64
	MCG–6-30-15	0.008	42.99	6.2	50664.14–50665.14	15	4.33	106
					50665.15–50666.15	15	4.47	104
					50666.15–50667.15	15	4.50	101
					50667.16–50668.15	15	5.08	90
					50668.16–50669.15	15	4.38	94
					50669.16–50670.16	15	4.04	94
					50670.16–50671.16	15	4.00	77
					50671.16–50672.16	15	5.01	99
					51378.13–51379.12	15	4.69	61
					51379.13–51380.12	15	5.41	72
					51380.13–51381.12	15	5.56	66
					51381.13–51382.12	14	6.74	77
					51382.13–51383.12	14	5.30	77
					51383.13–51384.12	15	5.48	68
					51384.13–51385.12	15	5.86	70
					51385.13–51386.13	15	5.61	75
					51386.14–51387.13	15	4.69	68
					51387.13–51388.13	15	5.58	68
					51736.06–51737.06	13	4.37	42
					51930.73–51931.58	13	5.55	76
	NGC 3227	0.004	42.20	$7.56^{+0.06}_{-0.08}$	50405.69–50406.68	12	6.05	135
					50406.69–50407.69	15	5.68	129
					50407.69–50408.69	15	5.44	114
					50408.76–50409.56	12	5.32	130
	NGC 4051	0.002	41.44	$5.7^{+0.3}_{-0.4}$	50430.43–50431.42	14	0.67	17
					50431.82–50432.82	15	1.72	33
					51626.99–51627.99	14	1.81	28
					52044.39–52045.38	15	2.11	27
					52046.51–52047.50	15	2.11	28
6 d	3C 120	0.033	44.24	$7.48^{+0.21}_{-0.28}$	52621.94–52627.95	24	5.57	71
	Fairall 9	0.047	44.17	$7.92^{+0.11}_{-0.32}$	52144.89–52150.93	22	2.54	20
					52151.00–52157.04	22	2.44	17
					52157.17–52163.21	21	2.75	26
					52163.34–52169.45	23	2.22	22
					52169.58–52175.62	23	2.07	23
	IC 4329a	0.016	43.99	$6.85^{+0.55}_{-6.85}$	52830.79–52836.65	27	13.08	72
					52837.05–52843.17	27	11.46	62
					52843.37–52849.30	30	12.33	63
					52849.50–52855.75	26	12.75	65
					52855.95–52862.08	24	12.79	65
	Mkn 279	0.030	43.82	7.4	52412.32–52418.07	18	1.44	18
	NGC 5548	0.017	43.63	$7.97^{+0.08}_{-0.07}$	52091.66–52097.70	22	5.95	48
					52097.77–52103.87	23	6.26	51
					52104.01–52109.98	23	5.30	45
					52110.11–52116.22	23	4.55	37
					52116.35–52122.46	22	3.19	26
	Ark 564	0.025	43.62	6.1	51694.85–51700.85	23	2.27	20

TABLE 1—*Continued*

Time Scale	Source Name	z	$\log(L_{2-12})$ (erg s^{-1})	$\log(M_{BH})$ ($M_\odot$)	MJD Range	Num. Pts.	Mean c s^{-1}	Mean S/N
					51700.98–51707.04	22	2.02	17
					51707.17–51713.50	25	2.20	18
					51713.50–51719.56	22	2.22	21
					51719.69–51725.68	21	2.26	20
	NGC 7469	0.016	43.38	$6.88^{+0.29}_{-6.88}$	50244.07–50250.09	24	3.26	59
					50250.15–50256.17	25	2.92	45
					50256.30–50262.38	25	2.65	60
					50262.45–50268.46	24	3.41	88
					50268.53–50274.55	25	3.01	71
	NGC 3783	0.010	43.31	$6.94^{+0.05}_{-0.06}$	51960.17–51966.28	24	6.13	43
					51966.41–51972.53	23	6.27	46
					51972.66–51978.64	21	6.44	43
	MCG–6-30-15	0.008	42.99	6.2	50664.18–50670.19	24	4.46	90
					51378.16–51384.16	24	5.45	70
					51622.71–51628.97	23	5.13	58
					51629.43–51635.43	18	4.26	50
					51635.70–51641.69	23	4.74	57
					51642.22–51648.22	22	4.96	53
					51648.42–51654.41	20	4.07	43
					51654.68–51660.61	20	4.65	39
					51661.27–51667.27	22	4.26	40
					51667.40–51673.40	18	4.98	51
					51673.60–51679.66	21	4.91	44
					51679.86–51685.78	21	4.52	35
	NGC 4151	0.003	42.59	$7.08^{+0.23}_{-0.38}$	51870.64–51876.69	24	8.26	43
					51876.75–51882.74	21	8.87	52
					51882.80–51888.86	22	8.93	63
					51889.12–51895.10	22	7.12	53
					51895.24–51901.22	23	7.92	64
	NGC 3227	0.004	42.20	$7.56^{+0.06}_{-0.08}$	51636.59–51642.51	22	3.69	43
					51642.85–51648.91	23	3.07	39
					51649.11–51655.04	21	2.58	33
					51655.30–51661.30	17	0.99	14
					51661.56–51667.63	23	0.89	11
					51667.96–51674.09	20	1.35	17
					51674.62–51680.81	19	1.34	14
					51681.01–51687.07	23	2.52	23
					51687.34–51693.33	22	3.06	27
					51693.60–51699.60	21	3.49	33
	NGC 4051	0.002	41.44	$5.7^{+0.3}_{-0.4}$	51665.34–51671.34	24	2.25	27
					51671.54–51677.60	19	2.09	24
					51678.06–51684.06	24	2.82	24
					51684.12–51690.05	23	4.20	31
					51690.38–51696.64	24	3.76	32
					51696.91–51702.90	23	2.89	24
					51703.10–51709.36	26	3.04	23
					51709.63–51716.55	23	3.23	24
					51717.15–51723.27	23	2.36	20
					51723.34–51729.33	18	2.38	17
					52042.36–52048.34	19	2.19	27
36 d	3C 390.3	0.056	44.48	$8.57^{+0.12}_{-0.48}$	50220.63–50257.05	23	2.72	70
	3C 120	0.033	44.24	$7.48^{+0.21}_{-0.28}$	50458.53–50494.49	22	5.80	107

TABLE 1—*Continued*

Time Scale	Source Name	z	$\log(L_{2-12})$ (erg s^{-1})	$\log(M_{BH})$ ($M_\odot$)	MJD Range	Num. Pts.	Mean c s^{-1}	Mean S/N
	Fairall 9	0.047	44.17	$7.92^{+0.11}_{-0.32}$	52144.89–52179.00	22	2.38	20
	IC 4329a	0.016	43.99	$6.85^{+0.55}_{-6.85}$	50665.82–50701.87	22	13.14	167
					52830.79–52864.84	22	12.61	63
	NGC 5548	0.017	43.63	$7.97^{+0.08}_{-0.07}$	52091.66–52125.44	22	4.97	42
	Ark 564	0.025	43.62	6.1	51694.85–51726.48	20	2.29	21
	NGC 7469	0.016	43.38	$6.88^{+0.29}_{-6.88}$	50244.07–50276.02	21	3.04	62
	NGC 3516	0.009	43.00	$7.23^{+0.07}_{-0.10}$	50523.03–50556.60	21	6.18	85
					50557.13–50590.94	22	4.43	65
					50591.01–50624.88	25	3.90	51
					50627.04–50659.11	21	4.08	52
	MCG–6-30-15	0.008	42.99	6.2	51622.71–51655.68	21	4.50	47
					51655.95–51688.58	20	4.49	38
	NGC 4151	0.003	42.59	$7.08^{+0.23}_{-0.38}$	51870.64–51904.88	22	8.84	58
	NGC 3227	0.004	42.20	$7.56^{+0.06}_{-0.08}$	51636.59–51669.36	22	2.16	27
					51669.62–51702.59	21	2.64	24
	NGC 4051	0.002	41.44	$5.7^{+0.3}_{-0.4}$	51665.34–51698.11	21	3.05	29
					51698.24–51731.00	21	2.68	19
216 d	PG 0804+761	0.1	44.59	8.21 ± 0.04	51610.61–51826.75	39	1.28	17
	3C 390.3	0.056	44.48	$8.57^{+0.12}_{-0.48}$	51186.05–51402.29	38	2.24	34
					51405.14–51621.49	38	3.99	58
					51624.78–51840.56	37	3.98	50
	3C 120	0.033	44.24	$7.48^{+0.21}_{-0.28}$	50812.09–51034.89	23	4.46	59
					51039.95–51256.43	32	4.89	65
					51260.23–51479.30	31	5.31	55
					52334.94–52550.15	32	4.82	37
	Fairall 9	0.047	44.17	$7.92^{+0.11}_{-0.32}$	50390.63–50598.35	36	2.81	56
					50604.01–50808.01	36	2.42	47
					51180.59–51393.78	46	1.79	26
					51398.20–51611.51	49	1.42	21
					51615.81–51829.08	46	1.33	15
					51833.52–52046.64	50	1.49	16
					52050.96–52264.31	44	2.51	23
					52268.55–52481.78	46	2.56	26
					52486.19–52699.54	42	2.01	19
	Ark 120	0.032	44.02	$8.27^{+0.09}_{-0.11}$	51026.23–51242.33	39	3.17	48
					51425.10–51644.10	40	3.28	40
	IC 4329a	0.016	43.99	$6.85^{+0.55}_{-6.85}$	52831.32–53048.37	38	13.72	78
	Mkn 110	0.035	43.88	$6.89^{+0.13}_{-0.21}$	51610.59–51830.22	22	2.02	22
	Mkn 590	0.026	43.83	$7.14^{+0.10}_{-0.09}$	51684.46–51905.06	26	3.42	28
	NGC 5548	0.017	43.63	$7.97^{+0.08}_{-0.07}$	50208.07–50426.16	29	6.12	70
					50437.54–50649.39	17	4.30	70
					50661.14–50871.76	15	5.60	83
					50886.70–51095.11	20	6.87	100
					51110.70–51328.96	40	6.39	73
					51333.20–51550.72	48	5.99	63
					51554.98–51772.72	48	3.66	40
					51776.90–51994.44	46	4.24	39
					51998.80–52216.32	45	3.39	32
					52220.63–52438.20	43	3.28	30
					52442.49–52659.94	47	1.69	18
	Ark 564	0.025	43.62	6.1	51179.58–51392.92	43	1.85	26
					51397.23–51610.51	44	1.86	23

TABLE 1—*Continued*

Time Scale	Source Name	z	$\log(L_{2-12})$ (erg s^{-1})	$\log(M_{BH})$ ($M_\odot$)	MJD Range	Num. Pts.	Mean c s^{-1}	Mean S/N
					51614.75–51827.95	41	1.76	16
					51832.24–52045.71	47	1.88	17
					52050.01–52263.32	45	1.90	16
					52267.61–52485.13	48	1.74	16
					52489.41–52702.88	46	1.78	18
	Mkn 335	0.026	43.62	$6.58^{+0.14}_{-0.13}$	51661.98–51880.63	23	2.14	21
	Mkn 79	0.022	43.46	$8.01^{+0.14}_{-0.35}$	51610.59–51830.22	22	1.84	20
	NGC 7469	0.016	43.38	$6.88^{+0.29}_{-6.88}$	52737.04–52954.51	43	2.94	25
	NGC 3783	0.010	43.31	$6.94^{+0.05}_{-0.06}$	51180.55–51398.15	49	7.89	82
					51402.34–51615.79	47	7.80	77
					51624.30–51841.91	45	8.11	62
					51846.14–52063.78	47	7.73	56
					52068.06–52289.92	47	7.80	55
	NGC 3516	0.009	43.00	$7.23^{+0.07}_{-0.10}$	50523.03–50731.55	41	4.52	57
					50740.07–50949.15	35	5.83	79
					50953.41–51162.41	46	4.19	64
					51166.60–51375.86	46	3.74	50
					51379.80–51593.40	47	2.78	44
	MCG–6-30-15	0.008	42.99	6.2	50411.95–50622.44	15	4.81	64
					50639.80–50858.59	17	5.20	66
					51870.90–52076.48	37	4.89	38
					52078.47–52284.63	31	5.65	40
					52286.87–52491.84	37	5.43	42
					52494.67–52701.47	32	5.31	40
	NGC 4151	0.003	42.59	$7.08^{+0.23}_{-0.38}$	51179.56–51397.20	50	18.31	139
					51401.48–51619.06	47	16.49	121
					51623.29–51840.99	49	18.47	101
	NGC 3227	0.004	42.20	$7.56^{+0.06}_{-0.08}$	51180.48–51382.74	31	4.92	60
					51447.16–51663.36	32	3.02	40
					51663.56–51879.93	27	2.10	20
					52174.71–52390.56	38	4.19	35
					52392.54–52609.78	30	4.38	37
	NGC 4051	0.002	41.44	$5.7^{+0.3}_{-0.4}$	50196.52–50411.78	26	2.95	36
					50427.85–50647.05	18	2.02	31
					50663.15–50888.20	17	1.11	18
					50899.34–51124.11	17	1.34	22
					51137.92–51365.04	20	1.91	26
					51394.87–51609.53	15	1.98	29
					51611.45–51828.02	41	2.17	19
					51829.15–52045.39	39	1.25	11
					52045.42–52262.34	38	2.11	19
					52264.38–52478.81	38	2.51	23
					52480.99–52698.63	43	2.46	20
1296 d	3C 120	0.033	44.24	$7.48^{+0.21}_{-0.28}$	50458.53–51563.21	25	5.07	71
	Fairall 9	0.047	44.17	$7.92^{+0.11}_{-0.32}$	51180.59–52477.68	39	1.86	22
	NGC 5548	0.017	43.63	$7.97^{+0.08}_{-0.07}$	50208.07–51473.99	40	5.66	71
					51478.23–52749.70	38	3.51	35
	Ark 564	0.025	43.62	6.1	51179.58–52476.67	38	1.86	18
	NGC 3783	0.010	43.31	$6.94^{+0.05}_{-0.06}$	51180.55–52375.11	35	7.85	59
	NGC 3516	0.009	43.00	$7.23^{+0.07}_{-0.10}$	50523.03–51819.48	35	4.22	58
	MCG–6-30-15	0.008	42.99	6.2	50159.80–51423.91	41	5.13	61
					51455.99–52701.47	37	5.62	42

TABLE 1—*Continued*

Time Scale	Source Name	z	$\log(L_{2-12})$ (erg s^{-1})	$\log(M_{BH})$ ($M_\odot$)	MJD Range	Num. Pts.	Mean c s^{-1}	Mean S/N
	NGC 3227	0.004	42.20	$7.56^{+0.06}_{-0.08}$	51180.48–52476.57	34	3.20	30
					50196.52–51438.88	39	1.76	25
	NGC 4051	0.002	41.44	$5.7^{+0.3}_{-0.4}$	51448.15–52702.59	38	1.92	18

Note. — The targets are ranked by 2–12 keV luminosity (col. [4]). Redshifts (col. [3]) were obtained from the NED database. All black hole mass estimates (Col. [4]) are reverberation-mapped masses from Kaspi et al. (2000) and Wandel, Peterson & Malkan (1999) except NGC 4051, from Shemmer et al. (2003), NGC 3783, from Onken & Peterson (2002), NGC 4593, NGC 3516 & NGC 3227, from Onken et al. (2003), and Mkn 279, from Wandel (2002) and Santos Lleo et al. (2001). Mass estimates for Ark 564, Mkn 766, MCG–6-30-15, MCG–2-58-22 are from Bian & Zhao (2003). The mass estimate for PKS 0558–504 is from Wang et al. (2001) and based on the empirical Kaspi et al. (2000) relation between optical luminosity and BLR size. Col. (7) is the number of points in the light curve after clipping and resampling to a common sampling rate. Col. (8) is the mean 2–12 keV count rate per PCU. Col. (9) is the signal-to-noise.

TABLE 2
ASCA SAMPLING PARAMETERS

Source Name	MJD Date Range	Sequence ID Number	Num. Pts.	Mean c s^{-1}	Mean S/N
3C 111	50126.54–50127.49	74087000	15	0.74	34
PG 0804+761	50756.55–50757.55	75058000	15	0.22	21
3C 390.3	49307.84–49308.94	70005000	15	0.35	24
Mkn 509	49471.39–49472.39	71013000	15	1.02	39
3C 120	49400.66–49401.66	71014000	15	1.06	45
MCG–2-58-22	49132.89–49133.70	70004000	13	0.24	12
	50600.47–50601.47	75049000	15	0.71	33
	50797.98–50798.98	75049010	15	0.70	33
Fairall 9	49688.22–49688.89	73011000	11	0.61	22
Ark 120	49624.79–49625.79	72000000	15	0.65	31
IC 4329a	49214.29–49215.24	70005000	15	1.54	42
NGC 5548	49195.65–49196.60	70018000	14	0.92	25
	50984.60–50985.60	76029010	15	1.57	44
	50985.60–50986.60	76029010	15	1.72	62
	50986.60–50987.60	76029010	15	1.54	32
Ark 564	50440.64–50441.64	74052000	15	0.57	23
NGC 7469	49323.32–49324.06	71028010	11	0.76	30
IRAS 18325–5926	49241.51–49242.51	70015000	15	0.13	9
	50534.59–50535.59	75024000	15	0.43	18
	50535.59–50536.59	75024000	15	0.44	21
	50536.59–50537.59	75024000	15	0.41	18
	50537.59–50538.59	75024000	15	0.35	17
	50538.59–50539.59	75024000	15	0.32	17
NGC 3783	50278.28–50278.96	74054020	11	1.55	41
Mkn 766	49339.13–49340.02	71046000	14	0.46	18
NGC 4593	49361.04–49362.04	71024000	13	0.76	34
NGC 3516	49444.15–49445.05	71007000	13	1.57	25
	50915.94–50916.94	76028000	15	0.87	36
	50916.94–50917.94	76028000	15	0.91	42
	50917.94–50918.94	76028000	15	0.89	37
	50918.94–50919.94	76028000	15	0.72	38
MCG–6-30-15	49177.27–49178.27	70016000	14	0.93	23
	49199.39–49200.39	70016010	15	0.76	21
	49556.25–49557.25	72013000	15	1.00	23
	49557.25–49558.25	72013000	15	1.29	21
	49558.25–49559.25	72013000	15	1.09	30
	49559.25–49560.25	72013000	15	0.88	27
	50663.95–50664.95	75006000	14	0.76	21
	50664.95–50665.95	75006000	15	0.84	25
	50665.95–50666.95	75006000	15	0.85	28
	50667.70–50668.70	75006010	15	0.75	25
	50668.70–50669.70	75006010	15	0.86	22
	50669.70–50670.70	75006010	14	0.69	22
NGC 4151	49847.14–49848.00	73019000	13	1.99	67
	49848.00–49848.80	73019000	12	2.42	69
	49848.80–49849.60	73019000	12	2.52	66
NGC 3227	49115.14–49116.12	70013000	15	0.78	37
	49852.06–49853.03	73068000	13	0.51	29
NGC 4051	49102.94–49103.89	70001000	14	0.28	13
	49510.61–49511.54	72001000	14	0.55	15
	49511.54–49512.47	72001000	14	0.51	15

Note. — Targets are ranked by 2–12 keV luminosity, given in Table 1. Col. (4) is the number of points in the *ASCA* light curve after orbitally binning. Col. (5) is the mean count rate averaged between both SIS instruments. The SIS data were unusable for the observation of NGC 4593 and the first observation of NGC 3227; the GIS data were used and GIS count rates were converted to SIS count rates using the online W3PIMMS tool.

TABLE 3
DERIVED VARIABILITY PARAMETERS FOR THE *RXTE* LIGHT CURVES

Time Scale	Source Name	2–12 keV F_{var} (%)	2–4 keV F_{var} (%)	7–12 keV F_{var} (%)	$\frac{2-4keV\,F_{var}}{7-12keV\,F_{var}}$
1 d	PKS 0558–504	12.1 ± 0.6	11.8 ± 0.9	13.9 ± 1.5	0.85 ± 0.11
	3C 111	1.1 ± 0.7	0.4 ± 2.2	1.4 ± 1.4	0.31 ± 1.58
	Mkn 509	1.5 ± 0.4	3.6 ± 0.8	Undef.	
	3C 120	4.0 ± 0.5	4.1 ± 0.9	4.5 ± 0.8	0.91 ± 0.27
	MCG–2-58-22	1.9 ± 0.4	2.9 ± 0.8	1.1 ± 2.8	2.67 ± 7.01
	Ark 120	6.2 ± 0.3	6.4 ± 0.5	6.8 ± 0.7	0.95 ± 0.12
	NGC 5548	5.7 ± 0.2	6.0 ± 0.3	5.6 ± 0.3	1.07 ± 0.08
	Ark 564	18.2 ± 0.5	18.0 ± 0.7	22.6 ± 1.5	0.80 ± 0.06
	NGC 7469	7.5 ± 0.5	8.6 ± 1.0	6.9 ± 1.3	1.26 ± 0.27
	IRAS 18325–5926	15.7 ± 0.5	15.9 ± 0.8	16.0 ± 1.1	1.00 ± 0.08
	NGC 3783	12.4 ± 0.3	16.7 ± 0.6	10.2 ± 0.5	1.63 ± 0.08
	Mrk 766	14.6 ± 0.8	15.5 ± 1.7	14.1 ± 2.2	1.09 ± 0.21
	NGC 4593	9.2 ± 0.5	10.2 ± 0.8	9.6 ± 0.9	1.05 ± 0.13
	NGC 3516	6.6 ± 0.2	8.2 ± 0.5	5.8 ± 0.5	1.42 ± 0.14
	MCG–6-30-15	17.9 ± 0.4	21.7 ± 0.6	15.3 ± 0.7	1.41 ± 0.08
	NGC 3227	12.6 ± 0.2	14.8 ± 0.4	11.0 ± 0.4	1.34 ± 0.06
	NGC 4051	32.0 ± 1.2	40.2 ± 2.6	26.5 ± 2.6	1.52 ± 0.18
6 d	3C 120	5.6 ± 0.3	5.2 ± 0.6	5.7 ± 0.6	0.92 ± 0.15
	Fairall 9	9.4 ± 1.2	8.8 ± 2.2	10.1 ± 2.9	0.88 ± 0.26
	IC 4329a	7.3 ± 0.3	7.7 ± 0.6	6.7 ± 0.6	1.15 ± 0.14
	Mkn 279	12.4 ± 1.6	14.1 ± 3.1	6.2 ± 4.3	2.27 ± 1.66
	NGC 5548	12.6 ± 0.6	13.5 ± 1.1	12.6 ± 1.2	1.07 ± 0.14
	Ark 564	31.6 ± 1.2	33.1 ± 1.5	30.2 ± 4.0	1.10 ± 0.15
	NGC 7469	12.3 ± 0.4	13.0 ± 0.7	11.8 ± 0.8	1.10 ± 0.10
	NGC 3783	12.8 ± 0.5	14.4 ± 1.0	12.1 ± 1.0	1.18 ± 0.26
	MCG–6-30-15	22.4 ± 0.5	27.1 ± 0.8	19.0 ± 1.0	1.43 ± 0.08
	NGC 4151	11.7 ± 0.4	13.2 ± 1.0	11.6 ± 0.7	1.13 ± 0.11
	NGC 3227	27.4 ± 1.3	33.1 ± 2.9	24.2 ± 2.5	1.37 ± 0.15
	NGC 4051	36.3 ± 0.9	43.1 ± 1.5	31.3 ± 2.0	1.38 ± 0.10
36 d	3C 390.3	27.5 ± 0.3	29.8 ± 0.6	25.8 ± 0.6	1.16 ± 0.04
	3C 120	8.0 ± 0.2	8.4 ± 0.4	8.4 ± 0.5	1.00 ± 0.08
	Fairall 9	12.5 ± 1.2	15.0 ± 2.2	11.9 ± 2.7	1.26 ± 0.34
	IC 4329a	11.7 ± 0.3	12.7 ± 0.5	10.7 ± 0.5	1.18 ± 0.07
	NGC 5548	25.6 ± 0.5	26.2 ± 0.9	25.4 ± 1.1	1.03 ± 0.06
	Ark 564	33.2 ± 1.1	33.3 ± 1.4	36.0 ± 3.5	0.92 ± 0.10
	NGC 7469	16.0 ± 0.4	17.9 ± 0.6	14.6 ± 0.8	1.23 ± 0.08
	NGC 3516	19.7 ± 0.4	26.5 ± 0.8	16.4 ± 0.7	1.61 ± 0.09
	MCG–6-30-15	25.5 ± 0.5	30.5 ± 0.9	22.7 ± 1.1	1.35 ± 0.08
	NGC 4151	24.5 ± 0.4	24.9 ± 1.0	24.7 ± 0.6	1.01 ± 0.05
	NGC 3227	52.6 ± 0.9	60.8 ± 1.8	46.3 ± 1.7	1.31 ± 0.06
	NGC 4051	41.3 ± 1.0	46.8 ± 1.5	36.7 ± 2.1	1.28 ± 0.08
216 d	PG 0804+761	14.2 ± 1.0	13.2 ± 1.6	10.2 ± 3.4	1.28 ± 0.45
	3C 390.3	22.0 ± 0.4	25.6 ± 0.7	20.3 ± 0.8	1.26 ± 0.06
	3C 120	16.9 ± 0.4	18.4 ± 0.7	16.0 ± 0.8	1.15 ± 0.07
	Fairall 9	22.7 ± 0.7	24.6 ± 1.3	20.8 ± 1.6	1.18 ± 0.11
	Ark 120	20.9 ± 0.4	22.9 ± 0.7	18.8 ± 0.9	1.22 ± 0.07
	IC 4329a	15.7 ± 0.2	17.0 ± 0.4	14.3 ± 0.4	1.19 ± 0.05
	Mkn 110	53.2 ± 1.0	57.4 ± 1.8	49.9 ± 2.2	1.15 ± 0.06
	Mkn 590	30.3 ± 0.8	32.5 ± 1.2	28.7 ± 1.5	1.13 ± 0.07
	NGC 5548	27.2 ± 0.4	28.9 ± 0.8	26.3 ± 0.9	1.10 ± 0.05
	Ark 564	27.7 ± 0.9	29.1 ± 1.1	29.1 ± 2.8	1.00 ± 0.10
	Mkn 335	32.0 ± 1.1	34.8 ± 1.5	28.5 ± 2.7	1.22 ± 0.13

TABLE 3—*Continued*

Time Scale	Source Name	2–12 keV F_{var} (%)	2–4 keV F_{var} (%)	7–12 keV F_{var} (%)	$\frac{2-4keV\,F_{var}}{7-12keV\,F_{var}}$
	Mkn 79	26.0 ± 1.2	27.4 ± 2.3	27.7 ± 2.6	0.99 ± 0.12
	NGC 7469	24.1 ± 0.6	25.7 ± 1.1	23.5 ± 1.3	1.09 ± 0.08
	NGC 3783	20.9 ± 0.2	24.0 ± 0.4	18.7 ± 0.5	1.28 ± 0.04
	NGC 3516	29.4 ± 0.3	38.4 ± 0.6	25.0 ± 0.6	1.54 ± 0.04
	MCG–6-30-15	25.7 ± 0.4	30.4 ± 0.7	22.2 ± 0.9	1.37 ± 0.06
	NGC 4151	32.3 ± 0.1	37.7 ± 0.3	30.0 ± 0.2	1.26 ± 0.01
	NGC 3227	34.9 ± 0.6	41.0 ± 1.3	30.4 ± 1.2	1.35 ± 0.07
	NGC 4051	61.7 ± 1.0	76.0 ± 1.7	51.8 ± 2.2	1.47 ± 0.07
1296 d	3C 120	18.5 ± 0.3	23.4 ± 0.6	17.7 ± 0.6	1.33 ± 0.06
	Fairall 9	38.2 ± 0.8	40.7 ± 1.2	37.2 ± 1.5	1.09 ± 0.06
	NGC 5548	31.6 ± 0.4	34.0 ± 0.7	30.0 ± 0.8	1.13 ± 0.04
	Ark 564	37.1 ± 1.0	42.5 ± 1.3	32.4 ± 3.0	1.31 ± 0.13
	NGC 3783	20.6 ± 0.3	22.7 ± 0.5	17.6 ± 0.6	1.29 ± 0.05
	NGC 3516	32.0 ± 0.3	40.0 ± 0.6	25.4 ± 0.6	1.57 ± 0.04
	MCG–6-30-15	24.5 ± 0.3	29.1 ± 0.6	19.9 ± 0.8	1.46 ± 0.06
	NGC 3227	56.3 ± 0.6	64.0 ± 1.2	48.5 ± 1.1	1.32 ± 0.04
	NGC 4051	61.7 ± 0.8	75.9 ± 1.4	51.1 ± 1.7	1.49 ± 0.06

Note. — Targets are ranked by 2–12 keV luminosity, given in Table 1. 1 d F_{var} for Mkn 279 is undefined at all bands and is not listed.

TABLE 4
DERIVED VARIABILITY PARAMETERS FOR THE *ASCA* LIGHT CURVES

Source Name	2–10 keV F_{var} (%)
PG 0804+761	3.2 ± 1.9
Mkn 509	4.0 ± 0.7
3C 120	1.5 ± 0.9
MCG–2-58-22	3.1 ± 1.0
Fairall 9	3.4 ± 2.3
Ark 120	2.7 ± 1.1
IC 4329a	5.6 ± 0.7
NGC 5548	6.5 ± 0.9
Ark 564	17.0 ± 1.2
NGC 7469	2.2 ± 1.5
IRAS 18325–5926	14.0 ± 1.9
NGC 3783	6.1 ± 0.8
Mkn 766	17.6 ± 1.6
NGC 4593	14.1 ± 0.9
NGC 3516	10.3 ± 0.9
MCG–6-30-15	20.0 ± 1.2
NGC 4151	6.3 ± 0.4
NGC 3227	14.8 ± 0.9
NGC 4051	29.6 ± 2.0

TABLE 5
SUMMARY OF BROADBAND VARIABILITY CORRELATIONS

Figure Number	x-axis	y-axis	Time Scale	No. Pts.	r	P_r	Slope
2	L_{2-12}	F_{var}	1 d (*ASCA*)	19	−0.737	3.19×10^{-4}	−0.345±0.018
			1 d (*RXTE*)	17	−0.676	2.89×10^{-3}	−0.316±0.022
			6 d	12	−0.744	5.53×10^{-3}	−0.223±0.018
			36 d	12	−0.673	1.60×10^{-2}	−0.175±0.018
			216 d	19	−0.687	1.16×10^{-4}	−0.139±0.008
			1296 d	9	−0.685	4.17×10^{-2}	−0.135±0.018
3	M_{BH}	F_{var}	1 d (*ASCA*)	18	−0.693	1.43×10^{-3}	−0.271±0.017
			1 d (*RXTE*)	15	−0.877	1.77×10^{-5}	−0.317±0.012
			6 d	12	−0.616	3.29×10^{-2}	−0.216±0.025
			36 d	12	−0.238	0.456	−0.066±0.025
			216 d	19	−0.504	2.78×10^{-2}	−0.101±0.010
			1296 d	9	−0.198	0.606	−0.042±0.026
4	$F_{var,soft}$	$F_{var,hard}$	1 d	16	+0.901	1.84×10^{-6}	+0.862±0.028
			6 d	12	+0.924	1.75×10^{-5}	+0.909±0.032
			36 d	12	+0.959	7.55×10^{-7}	+0.969±0.026
			216 d	19	+0.959	4.04×10^{-8}	+0.953±0.016
			1296 d	9	+0.957	5.21×10^{-5}	+0.986±0.037
5	$F_{var,soft}$ / $F_{var,hard}$	L_{2-12}	1 d	16	−0.614	1.14×10^{-2}	−0.238±0.009
			6 d	12	−0.664	1.85×10^{-2}	−0.138±0.013
			36 d	12	−0.275	0.387	−0.046±0.006
			216 d	19	−0.410	8.12×10^{-2}	−0.063±0.003
			1296 d	9	−0.519	0.152	−0.105±0.007
	$F_{var,soft}$ / $F_{var,hard}$	M_{BH}	1 d	14	+0.090	0.760	+0.033±0.009
			6 d	12	−0.658	2.00×10^{-2}	−0.162±0.016
			36 d	12	−0.140	0.664	−0.025±0.007
			216 d	19	−0.229	0.346	−0.049±0.005
			1296 d	9	−0.704	3.42×10^{-2}	−0.136±0.038

Note. — Col. (6) is the Pearson correlation coefficient. Col. (7) is the probability of obtaining correlation coefficient by chance.

TABLE 6
SUMMARY OF COLOR-FLUX DIAGRAMS

Source Name	MJD Range	⟨ HR ⟩	ϕ
PG 0804+761	51676–51971	0.71	0.813±0.026
3C 390.3	51261–51555	1.04	1.059±0.004
3C 120	52335–52635	1.08	1.042±0.005
Fairall 9 (1)	51679–51974	1.03	1.057±0.010
Fairall 9 (2)	51978–52268	0.97	1.116±0.009
Fairall 9 (3)	52277–52571	1.00	1.162±0.043
Ark 120	50868–51167	0.97	1.075±0.018
IC 4329a	52737–53035	1.10	1.178±0.008
NGC 5448 (1)	51678–51968	1.06	1.024±0.006
NGC 5548 (2)	51977–52271	1.06	1.032±0.003
NGC 5548 (3)	52276–52574	1.09	1.016±0.022
Ark 564 (1)	51678–51973	0.43	0.921±0.008
Ark 564 (2)	51977–52271	0.47	0.950±0.056
Ark 564 (3)	52276–52574	0.50	0.861±0.044
NGC 3783 (1)	51679–51975	1.19	1.188±0.009
NGC 3783 (2)	51976–52272	1.16	1.207±0.032
NGC 3516 (1)	50523–50799	1.40	1.388±0.004
NGC 3516 (2)	50838–51119	1.43	1.318±0.017
MCG–6-30-15 (1)	51676–51974	0.97	1.224±0.015
MCG–6-30-15 (2)	51976–52274	0.98	1.224±0.006
MCG–6-30-15 (3)	52276–52554	0.93	1.308±0.010
NGC 4151	51678–51964	2.08	1.075±0.003
NGC 3227 (1)	52000–52298	1.60	1.238±0.011
NGC 3227 (2)	52300–52599	1.31	1.269±0.019
NGC 4051 (1)	51676–51974	1.03	1.303±0.005
NGC 4051 (2)	51976–52274	1.03	1.241±0.010
NGC 4051 (3)	52276–52574	1.00	1.309±0.010

Note. — Col. (3) is the mean 7–12 keV / 2–4 keV count rate hardness ratio (HR) value for light curve, obtained from the binned data in Figure 6. Col. (4) lists ϕ, which quantifies the decrease in HR for every doubling in flux, as described in the text.

TABLE 7
SPECTRAL VARIABILITY MODEL PARAMETERS

Source Name	Pivot Energy (keV)	Median Γ (R=0/R=1)	2-comp. Γ_{int}	2-comp. median $A_R/A_{\Gamma_{int}}$
PG 0804+761	∞	2.4/2.5	2.3	0
3C 390.3	3000	2.0/2.1	2.0	0.5
3C 120	3000	2.0/2.1	2.0	0.3
Fairall 9	1000	2.1/2.2	2.1	1.3
Ark 120	3000	2.0/2.1	2.1	1.3
IC 4329a	1000	2.0/2.1	2.1	1.9
NGC 5548	3000	2.0/2.1	1.9	0.2
Ark 564	∞	2.7/2.8	2.7	0
NGC 3783	1000	1.9/2.0	2.1	2.0
NGC 3516	100	1.7/1.8	1.9	3.2
MCG–6-30-15	100	2.1/2.2	2.3	3.2
NGC 4151	3000	1.3/1.4	1.4	0.5
NGC 3227	1000	1.6/1.7	1.8	2.0
NGC 4051	100	2.1/2.2	2.3	3.2

Note. — Columns (2) and (3) are the approximate best model parameters for the spectral pivoting model of spectral variability. In Column (3), the values of Γ with relative reflection R=0 and R=1 are given. For PG 0804+761 and Ark 564, values were estimated using ϕ=1 (infinite pivot energy). Columns (4) and (5) are the approximate best model parameters for the two-component model (constant Γ_{int}, variable $A_R/A_{\Gamma_{int}}$). For PG 0804+761 and Ark 564, values were estimated using ϕ=1 ($A_R/A_{\Gamma_{int}} = 0$.

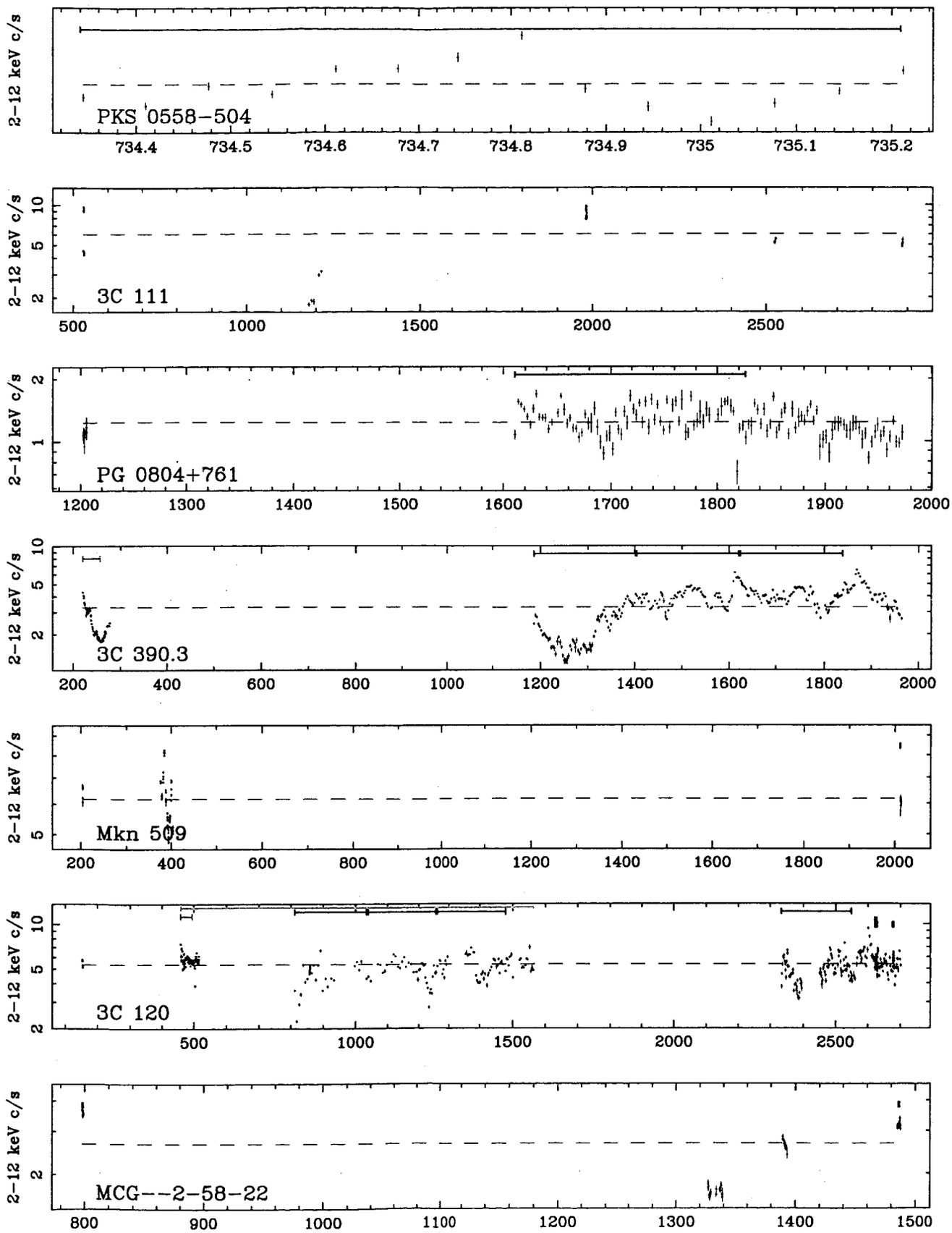

FIG. 1.— *RXTE* 2–12 keV total light curves, ranked by 2–12 keV luminosity, before clipping and resampling. The black, red, green, blue and orange bars denote the extent of the 1 d, 6 d, 36 d, 216 d, and 1296 d *RXTE* light curves, respectively, before subsampling to a common sampling rate. Error bars are 1σ.

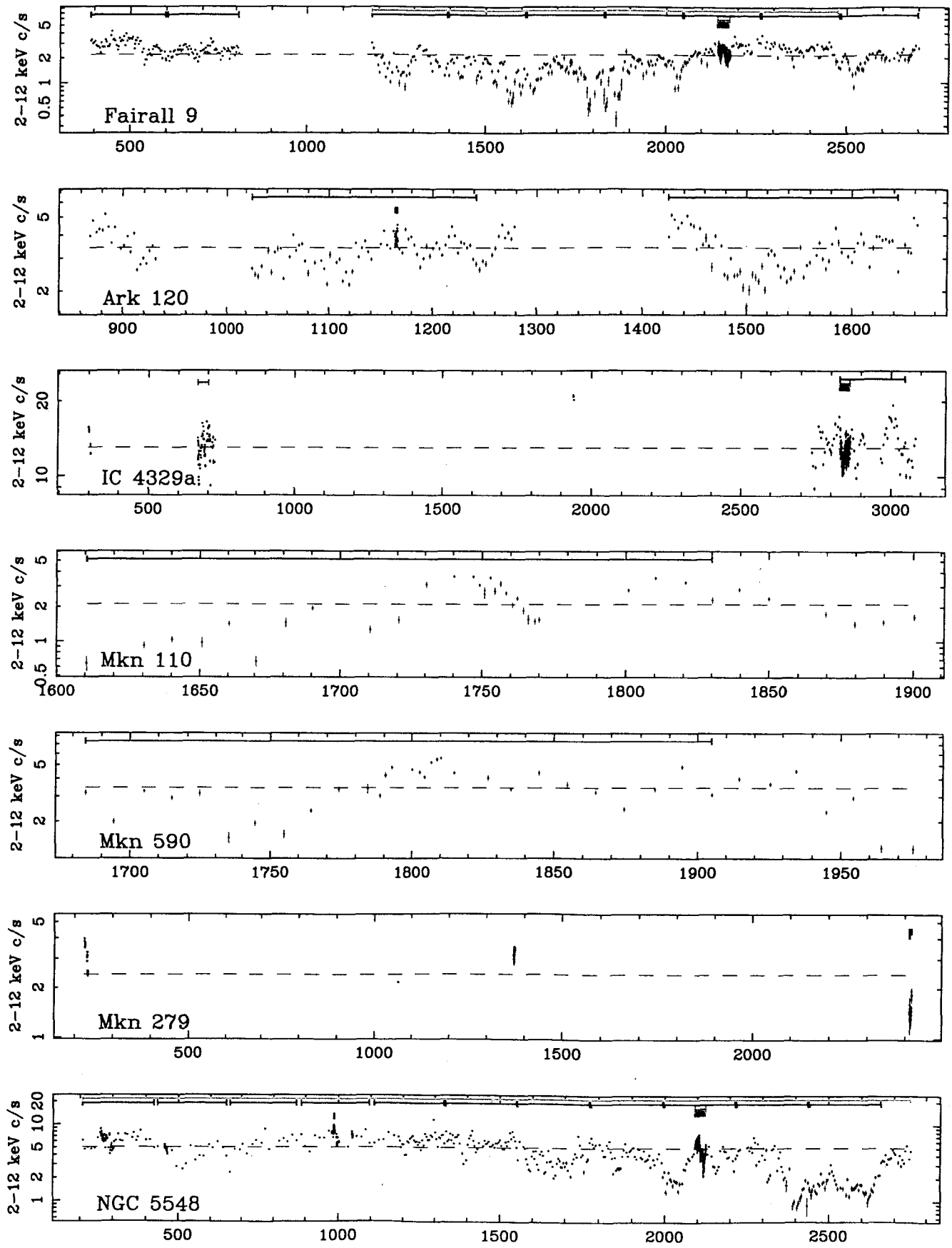

FIG. 1.— Figure 1, cont'd.

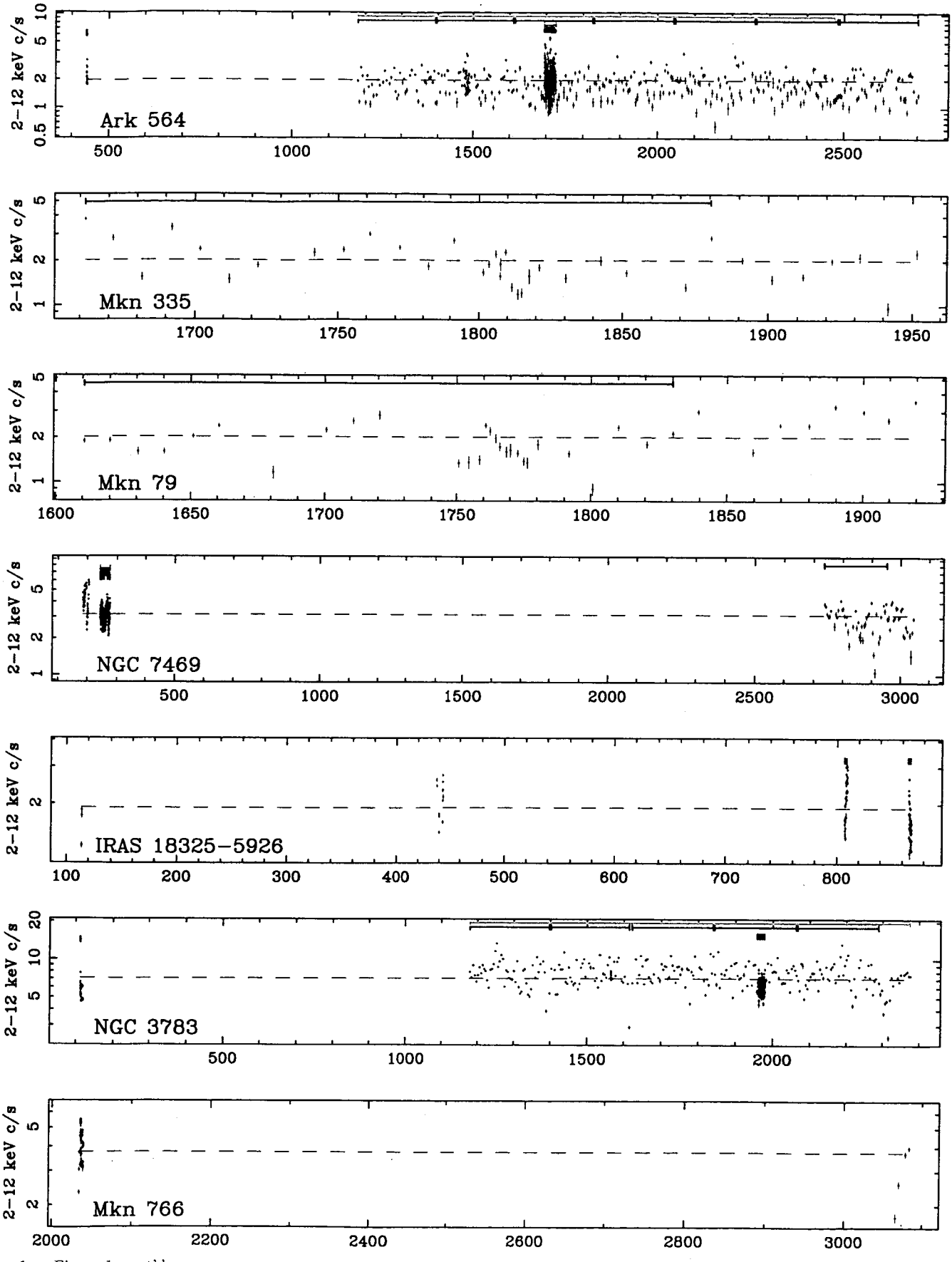

FIG. 1.— Figure 1, cont'd.

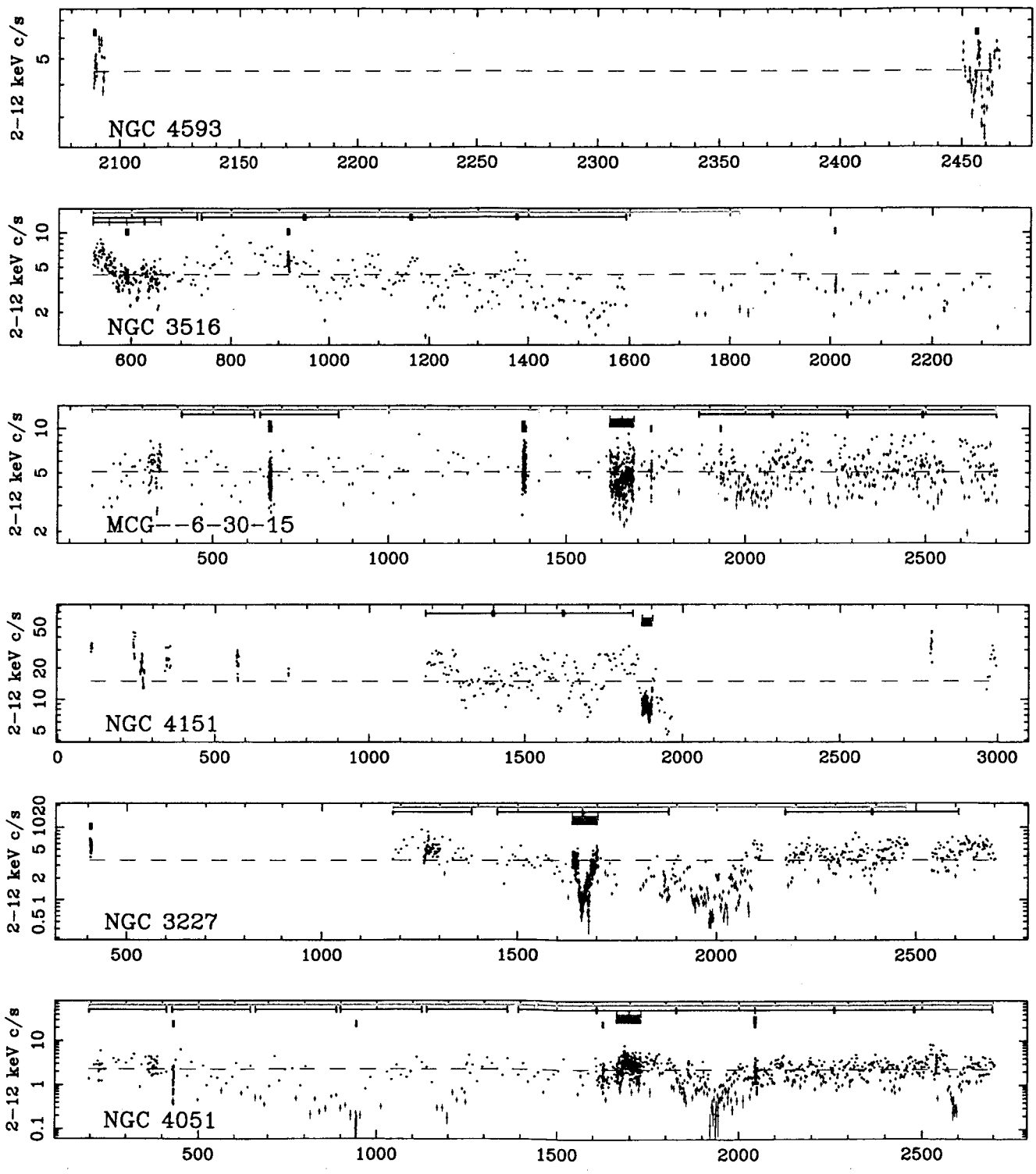

FIG. 1.— Figure 1, cont'd.

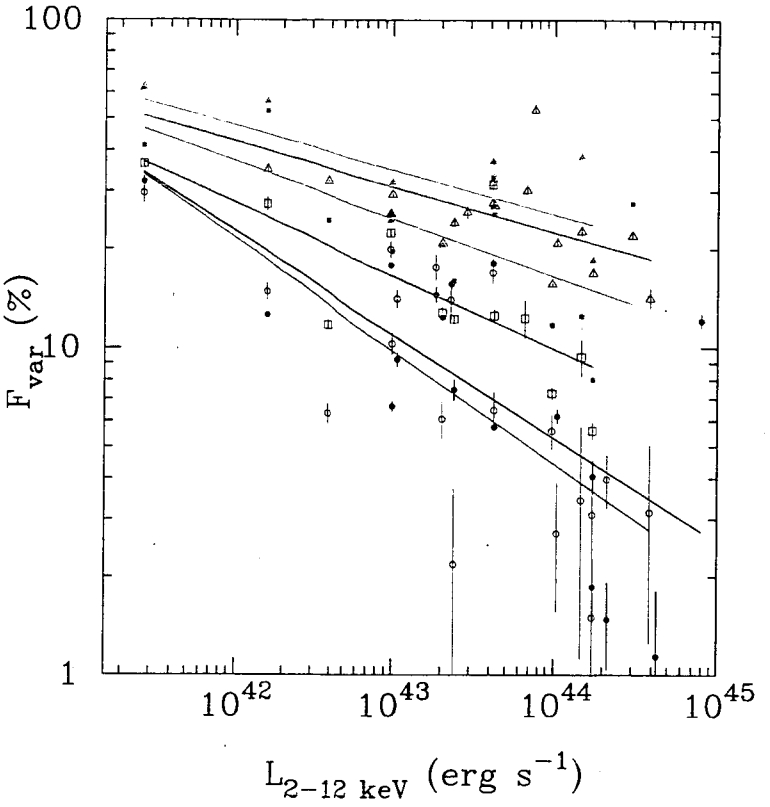

FIG. 2.— F_{var} plotted against 2–10 keV luminosity for all time scales. 1 d *ASCA*, 1 d *RXTE*, 6 d 36 d, 216 d, and 1296 d time scale data points are denoted by purple open circles, black filled circles, red open squares, green filled squares, blue open triangles, and orange filled triangles, respectively. The best-fit lines for each time scale are the same color.

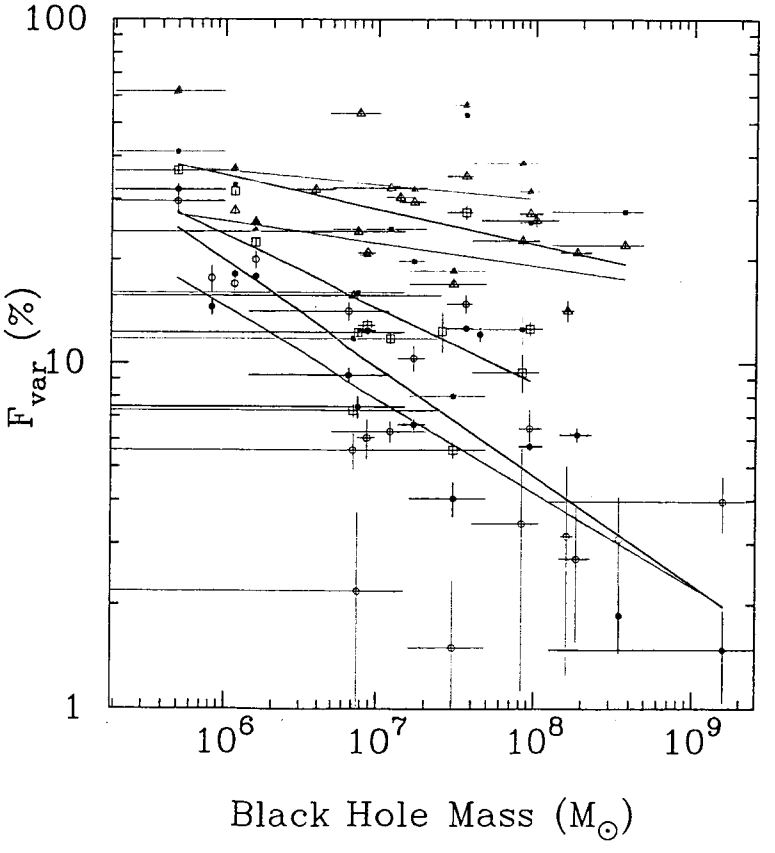

FIG. 3.— F_{var} plotted against black hole mass estimate M_{BH} for all time scales. Data points and best-fit lines are denoted the same as in Figure 2.

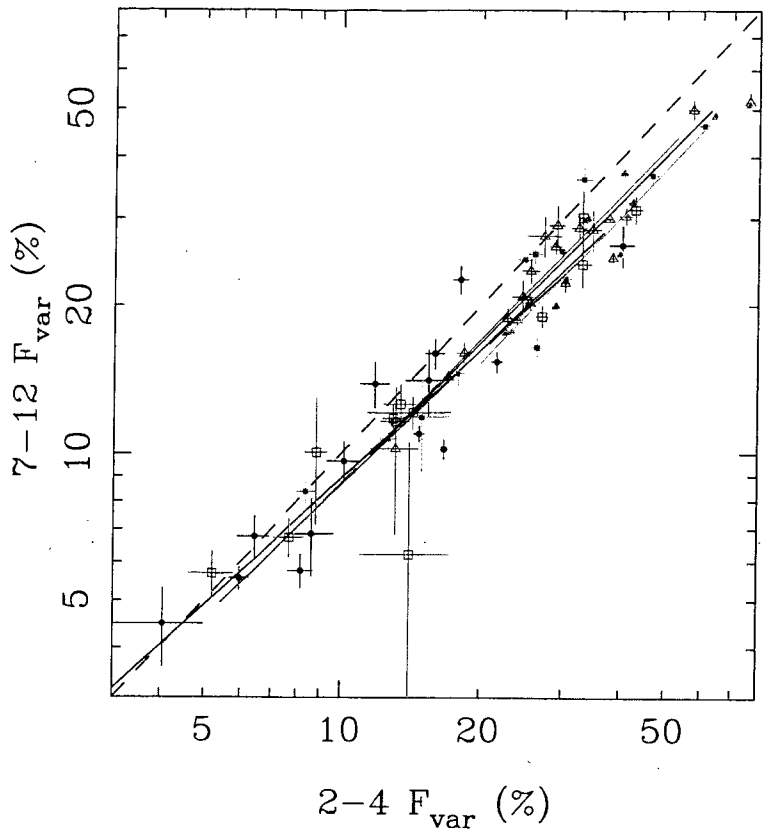

FIG. 4.— 7–12 keV F_{var} plotted against 2–4 keV F_{var}. Data points and best-fit lines are denoted the same as in Figure 2. A source with equally strong variability in the two bands would lie on the dashed line, but the vast majority of the light curves exhibit stronger variability in the softer band.

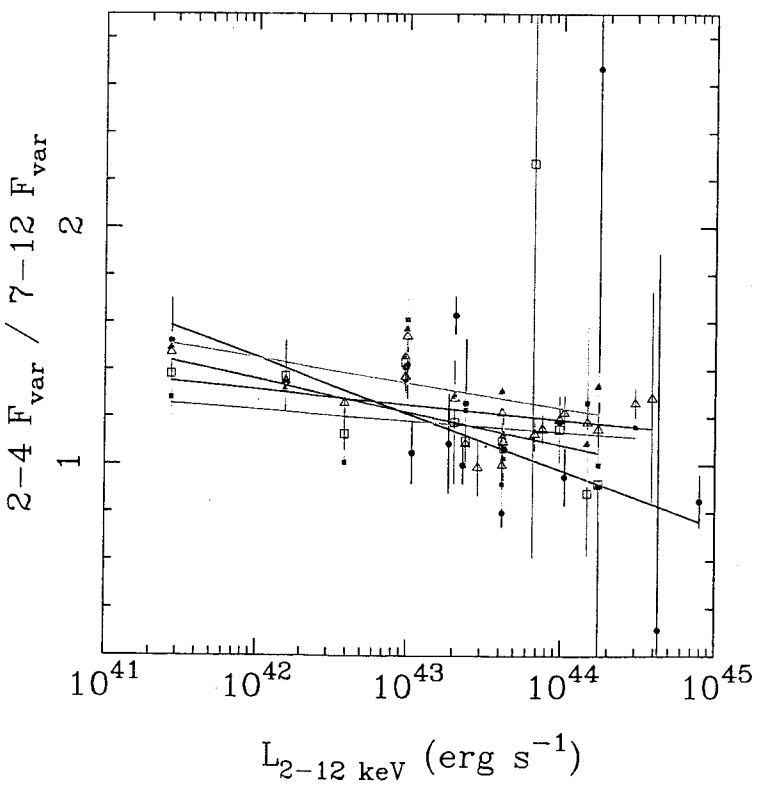

FIG. 5.— The ratio of 2–4 keV F_{var} / 7–12 keV F_{var} plotted against source luminosity. Data points and best-fit lines are denoted the same as in Figure 2. There is tentative evidence for relatively less luminous sources to display increasingly stronger variability in the soft band compared to the hard band.

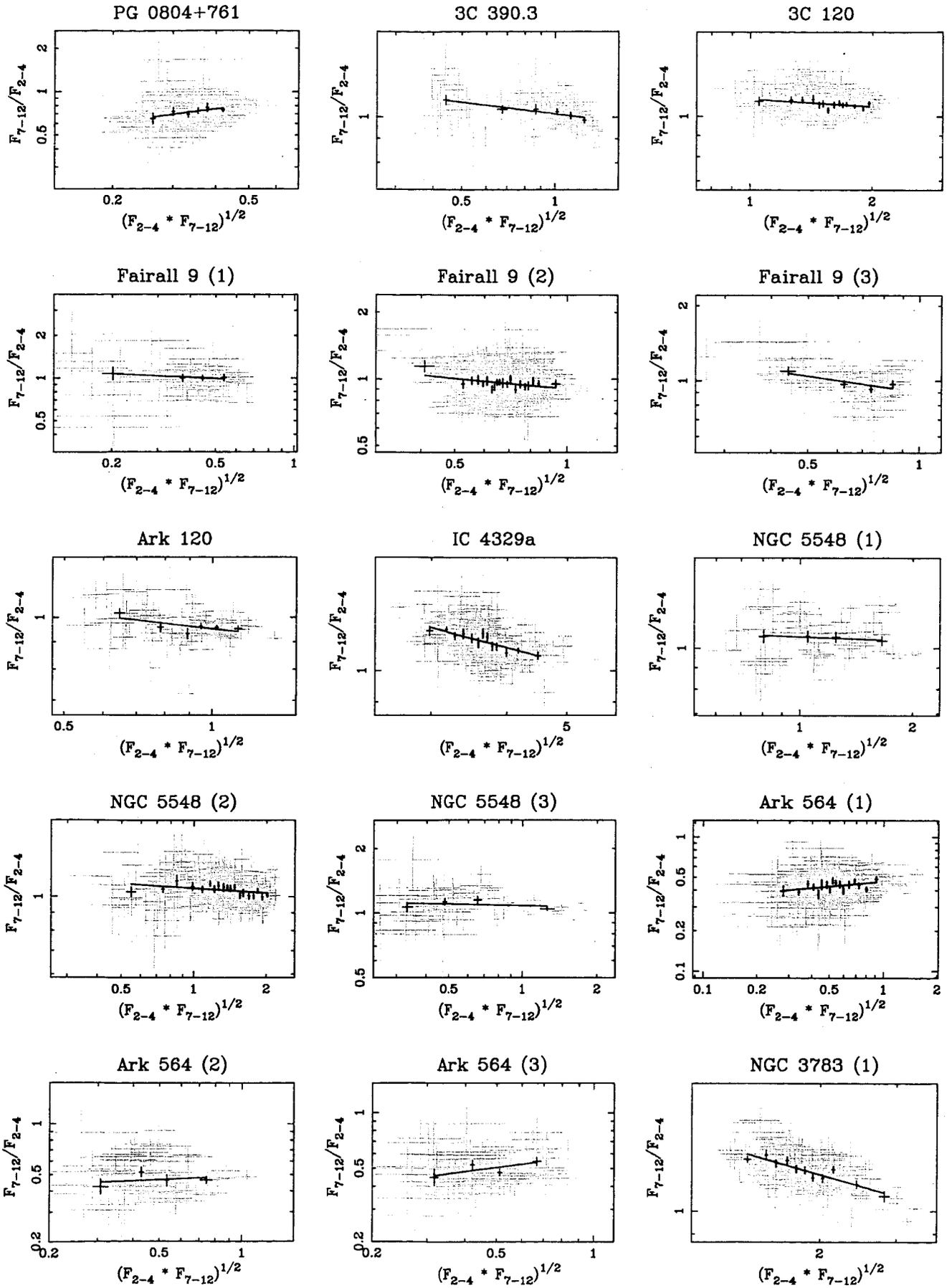

FIG. 6.— Plots of the 7–12 keV/2–4 keV hardness ratio (HR) against geomtric mean count rate for the 27 light curves with adequate data. Gray error bars represent the unbinned data; black points represent the binned data. The solid lines are the best linear fits to the binned data.

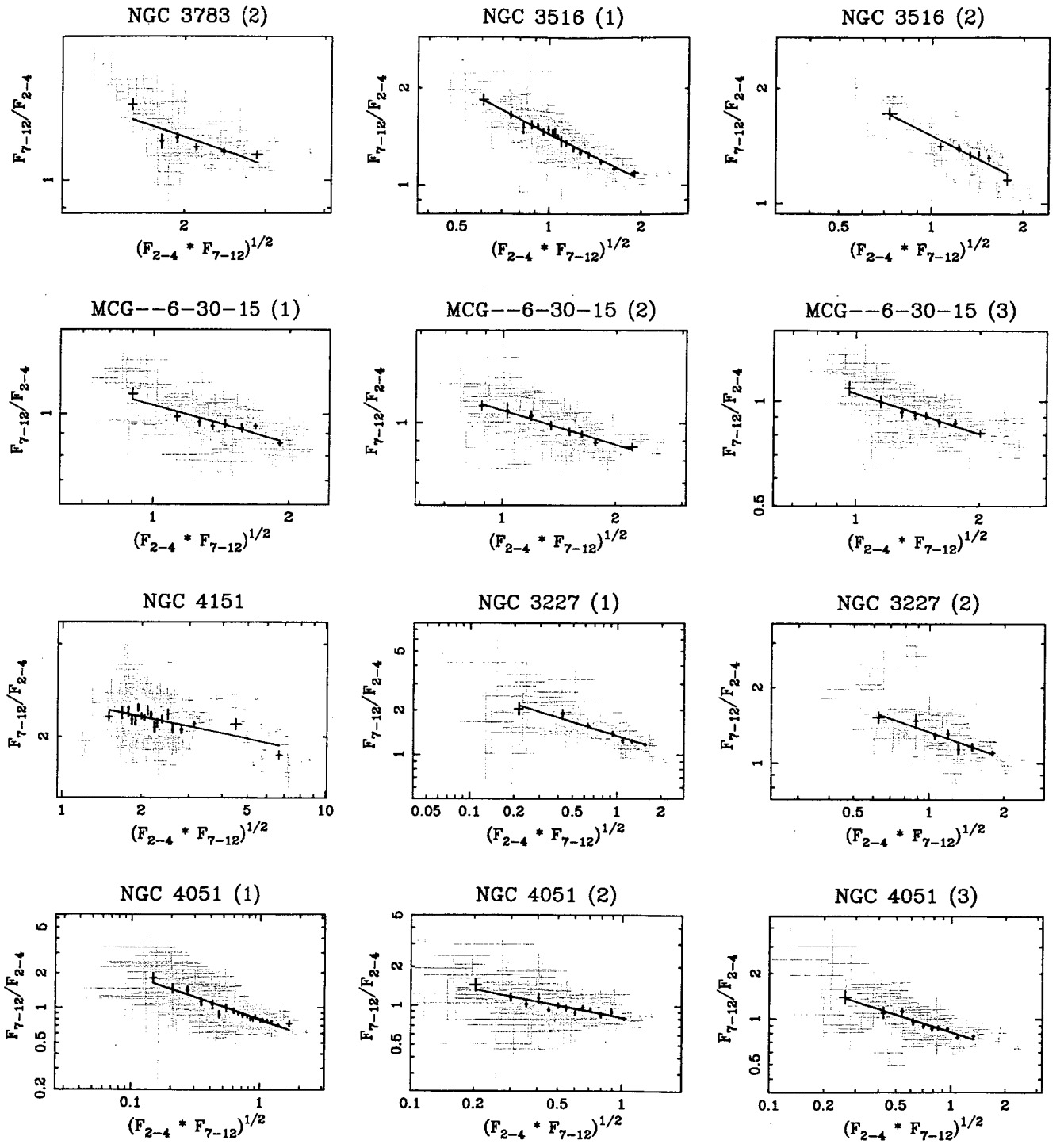

FIG. 6.— Continued.

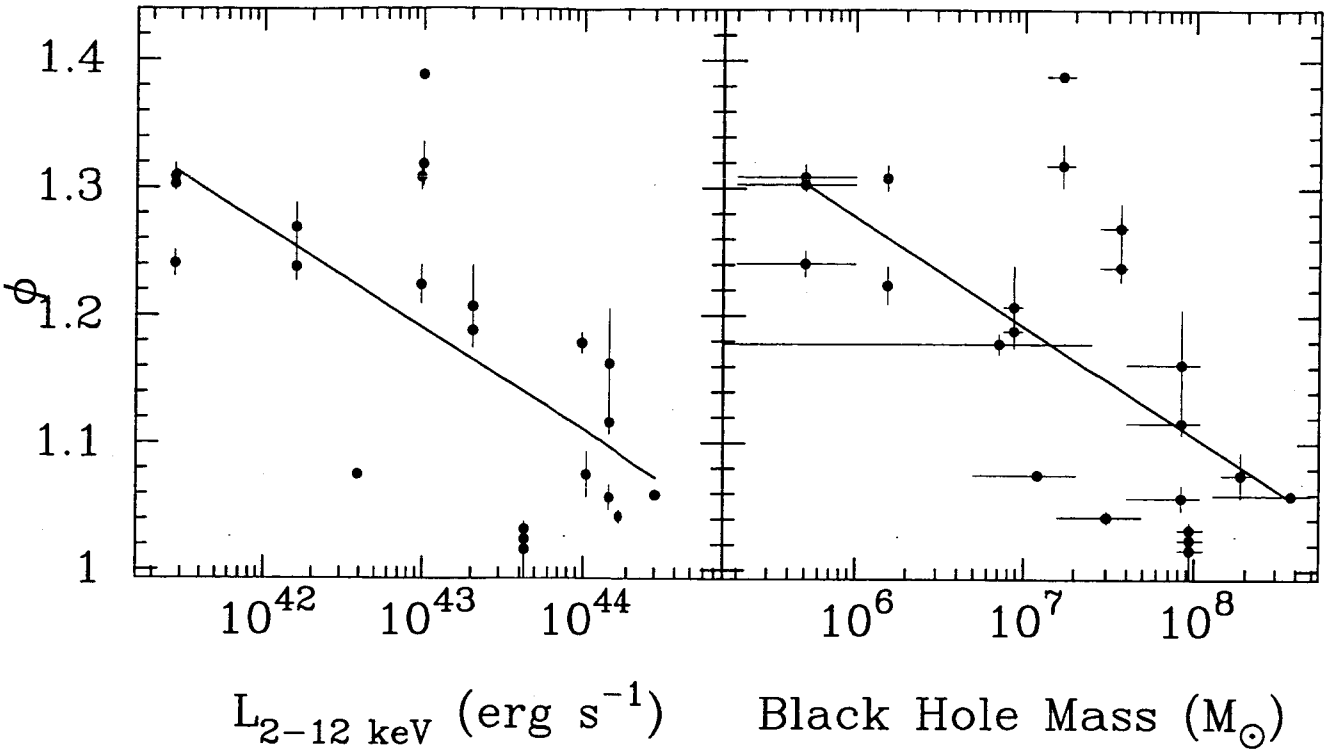

FIG. 7.— The parameter ϕ, which quantifies the decrease in 7–12 keV/2–4 keV hardness ratio (HR) for every doubling in flux, plotted against 2–12 keV luminosity and black hole mass estimate $M_{\rm BH}$. There is a tendency for relatively less luminous or less massive sources to display more overall spectral variability.

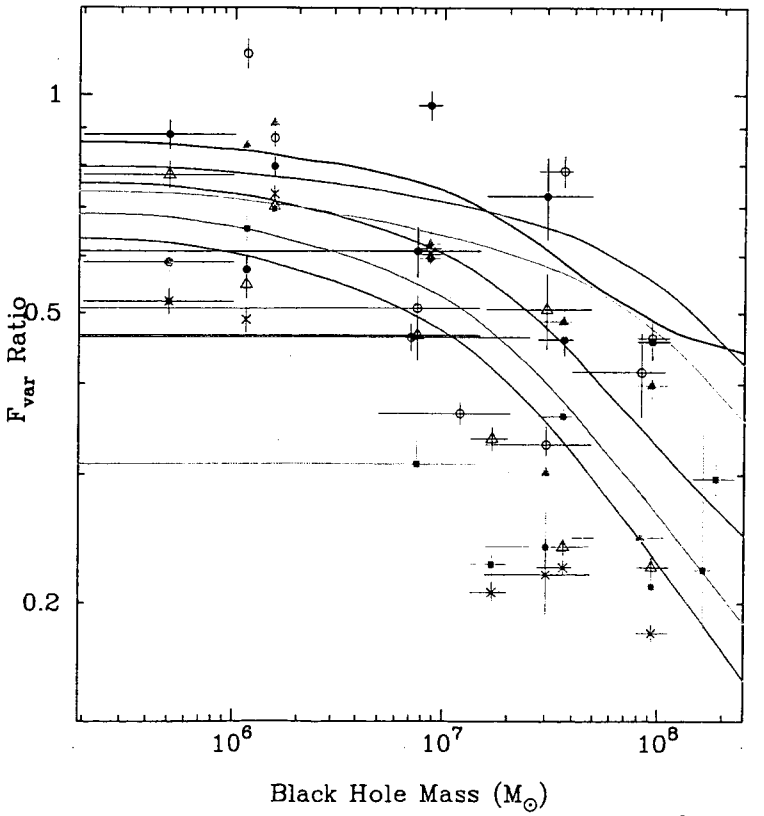

FIG. 8.— Predicted and measured ratios of F_{var} for six time scale combinations plotted against black hole mass estimate $M_{\rm BH}$. The measured ratios of 1 d/6 d, 1 d/36 d, 1 d/216 d, 1 d/1296 d, 6 d/216 d and 6 d/1296 d F_{var} are denoted by black filled circles, red open triangles, green filled squares, blue crosses, purple open circles and orange filled triangles, respectively. The predicted ratios were derived from linearly scaling the PSD break frequency with black hole mass using the best-fit relation $T_b = M_{\rm BH}/10^{7.05}\ M_\odot$.

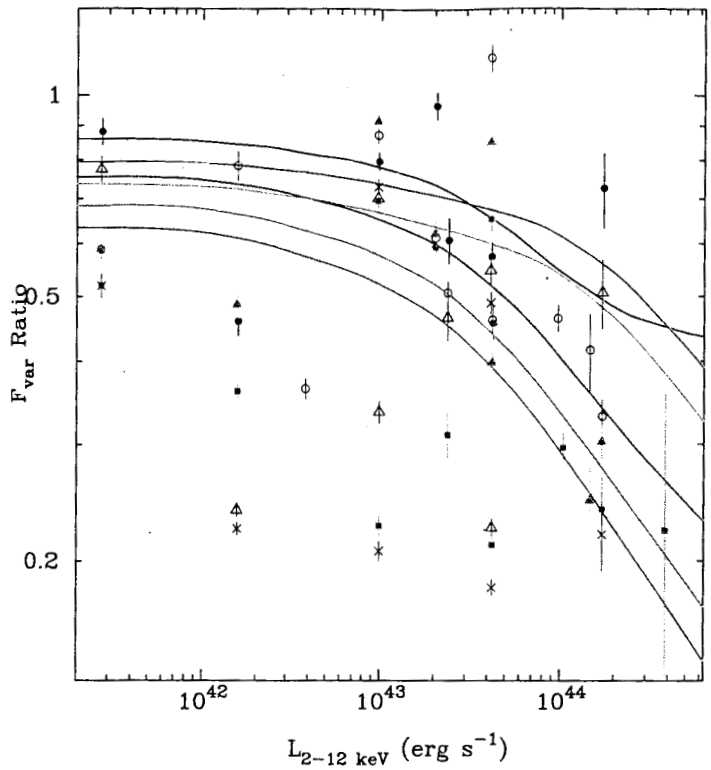

FIG. 9.— Predicted and measured ratios of F_{var} for six time scale combinations plotted against 2–12 keV luminosity. Data and best-fit models are denoted the same as in Figure 8. The predicted ratios were derived from linearly scaling PSD break frequency with bolometric luminosity using the best-fit relation $T_b = L_{2-12\ keV}/10^{43.35}$ erg s^{-1}.

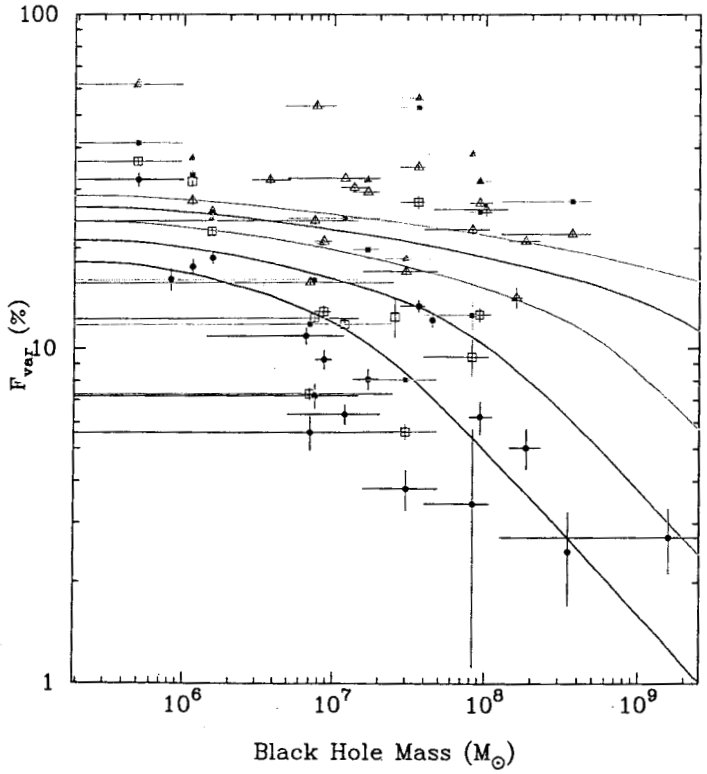

FIG. 10.— Measured and predicted values of 2–12 keV F_{var} plotted against black hole mass. 1 d, 6 d 36 d, 216 d, and 1296 d time scale data points are denoted by purple open circles, black filled circles, red open squares, green filled squares, blue open triangles, and orange filled triangles, respectively. The best-fit lines for each time scale are the same color. The predicted values were obtained using the best-fit T_b–M_{BH} relation from Figure 8; here they are best-fit in the y-direction to constrain PSD normalization A.